AGU PUBLICATIONS

JGR

Journal of Geophysical Research: Atmospheres

RESEARCH ARTICLE
10.1002/2014JD021975

Key Points:
- Wavelet analysis used to evaluate reanalysis
- Infrared flux by clouds biased low in reanalysis
- Spatial resolution is a factor in representing variability on short time scales

Supporting Information:
- Readme
- Texts S1 and S2 and Figures S1–S4

Correspondence to:
C. J. Cox,
christopher.cox-2@colorado.edu

Citation:
Cox, C. J., V. P. Walden, G. P. Compo, P. M. Rowe, M. D. Shupe, and K. Steffen (2014), Downwelling longwave flux over Summit, Greenland, 2010–2012: Analysis of surface-based observations and evaluation of ERA-Interim using wavelets, *J. Geophys. Res. Atmos.*, *119*, 12,317–12,337, doi:10.1002/2014JD021975.

Received 30 APR 2014
Accepted 15 OCT 2014
Accepted article online 17 OCT 2014
Published online 14 NOV 2014

Downwelling longwave flux over Summit, Greenland, 2010–2012: Analysis of surface-based observations and evaluation of ERA-Interim using wavelets

Christopher J. Cox[1,2,3,4], Von P. Walden[4,5], Gilbert P. Compo[1,3], Penny M. Rowe[4,6], Matthew D. Shupe[1,3], and Konrad Steffen[7]

[1]Cooperative Institute for Research in Environmental Sciences, University of Colorado, Boulder, Colorado, USA, [2]Department of Atmospheric and Oceanic Sciences, University of Colorado, Boulder, Colorado, USA, [3]Physical Sciences Division, NOAA Earth System Research Laboratory, Boulder, Colorado, USA, [4]Geography Department, University of Idaho, Moscow, Idaho, USA, [5]Department of Civil and Environmental Engineering, Washington State University, Pullman, Washington, USA, [6]Departamento de Física, Universidad de Santiago de Chile, Santiago, Chile, [7]Swiss Federal Institute for Forest, Snow, and Landscape Research (WSL), Zürich, Switzerland

Abstract This study analyzes the downwelling longwave radiation (DLW) over the Greenland Ice Sheet (GrIS) using surface-based observations from Summit Station (72°N, 38°W; 3210 m) and the European Centre for Medium-Range Weather Forecasts Interim Reanalysis (ERA-Interim) DLW fields. Since surface-based observations are sparse in the Arctic, the accuracy of including reanalyses for spatial context is assessed. First, the DLW at Summit is reported, including the significant time scales of variability using time-frequency decomposition (wavelet analysis). A new method for evaluating reanalyses is then introduced that also uses wavelet analysis. ERA-Interim DLW performs reasonably well at Summit, but because it includes too many thin clouds and too few thick clouds, it is biased low overall. The correlation between the observations and ERA-Interim drops from $r^2 > 0.8$ to near 0 for time series reconstructed from time scales less than ~4 days. These low correlations and additional analyses suggest that the spatial resolution of the data sets is a factor in representing variability on short time scales. The bias is low across all time scales and is thus likely tied to cloud generation processes in the model rather than the spatial representation of the atmosphere across the GrIS. The exception is autumn, when ERA-Interim overestimates the influence of clouds at time scales of 1 and 4 weeks. The spatial distribution of cloud influence on the DLW across the GrIS indicates that Summit is located in a transition zone with respect to cloud properties. The gradient across this transition zone is steepest near Summit in autumn, so the spatial characteristics of the atmosphere near Summit may contribute to the ERA-Interim bias during this time.

1. Introduction

Environmental changes are occurring in the Arctic. Among these changes are increasing boundary layer air temperatures [*Overland et al.*, 2008] and humidity [*Francis and Hunter*, 2007], which are associated with cloud feedback [*Liu et al.*, 2008; *Wang and Key*, 2005b]. Cryospheric responses include melting permafrost [*Osterkamp*, 2007] and reductions in summer sea ice extent and thickness [*Wang and Overland*, 2009; *Parkinson and Comiso*, 2013; *Zhang et al.*, 2013], which also feedback to the atmosphere [*Curry et al.*, 1996; *Schuur et al.*, 2008]. Changes in high-latitude atmospheric circulation have also been observed [*Zhang et al.*, 2008; *Wang et al.*, 2009]. The Greenland Ice Sheet (GrIS) may also be responding to the shifting climate. Its mass balance has become increasingly negative since the early 1990s [*Rignot and Kanagaratnam*, 2006] mainly because of increasing dynamic instability and ice loss from glaciers. Ablation and accumulation at the ice-atmosphere interface, representing the surface mass balance, have been characterized by coincident increases in runoff and precipitation [*Hanna et al.*, 2008; *Box*, 2013]. *Rignot et al.* [2008] report that mass balance from ice drainage is closely tied to the components of the surface mass balance. Over decadal time scales, changes in the sign of surface mass balance trends due to exchanges in the dominance of accumulation and runoff rates [*Box*, 2013] demonstrate the complexity of the system. The total mass loss may contribute to other climate changes, including sea level rise [*Alley et al.*, 2005], and modifications to the thermohaline circulation [*Fichefet et al.*, 2003].

Clouds are important modulators of the surface energy budget and mass balance of the GrIS. These modulations are caused by a combination of the net radiative effect of clouds [*Starkweather*, 2004] and precipitation [*Ohmura and Reeh*, 1991]. Recent studies have demonstrated that the downwelling longwave (DLW) component

of the radiation budget, and its relationship to clouds, is playing an important role in the observed changes in the Arctic [*Francis and Hunter*, 2006, 2007] and in extreme events, such as an anomalous surface melting event that occurred across the GrIS in July 2012 [*Bennartz et al*., 2013; *Neff et al*., 2014].

New measurements of the atmosphere above the GrIS, beginning in May 2010, are available from an atmospheric observatory at Summit Station (72°N, 38°W; 3210 m) called the Integrated Characterization of Energy, Clouds, Atmospheric state, and Precipitation at Summit (ICECAPS) [*Shupe et al*., 2013]. ICECAPS is modeled after the U.S. Department of Energy Atmospheric Radiation Measurement program observatories. Surface-based observations from ICECAPS provide high-quality measurements of cloud and atmospheric properties, including the DLW.

Spatial comparisons of cloud properties measured at multiple surface-based observatories have been made in recent studies [*Doran et al*., 2006; *de Boer et al*., 2009; *Shupe*, 2011; *Shupe et al*., 2011; *Cox et al*., 2014], including their DLW properties [*Cox et al*., 2012]. Studies of DLW and clouds at single observatories have also been conducted [*Intrieri et al*., 2002; *Dong and Mace*, 2003; *Shupe and Intrieri*, 2004; *Lesins et al*., 2009; *Dong et al*., 2010]. Collectively, these studies, in agreement with satellite observations [*Wang and Key*, 2005a; *Liu et al*., 2012], show that clouds are common in the Arctic but that there is spatial heterogeneity in cloud properties and their interactions with radiation.

Surface observatories represent point locations, so additional data sets are needed to provide spatial context for station observations. Reanalyses may be useful tools in providing this needed spatial information. DLW fields from reanalyses have been used previously for this purpose at Arctic observatories [*Cox et al*., 2012]. However, derived parameters from reanalysis data, such as surface radiative flux fields, remain largely a product of a short-term forecast generated by a numerical weather prediction model. As they do not rely directly on observations, they require evaluation. Furthermore, the spatial grids of reanalyses are coarse, and, therefore, the accuracy of reanalysis fields interpolated between grid points needs to be assessed. It is important to conduct thorough evaluations to assess reanalysis performance and to better understand the nature of the differences in the representativeness of the gridded and point data. Evaluation of reanalysis fields has been performed previously on cloud properties and radiative data in the Arctic. Evaluation studies of reanalyses that utilize a three-dimensional variational assimilation system showed that the cloud representation was problematic [e.g., *Walsh and Chapman*, 1998; *Bromwich et al*., 2007; *Walsh et al*., 2009; *Cox et al*., 2012], but *Cox et al*. [2012] and *de Boer et al*. [2014] reported that the European Centre for Medium-Range Weather Forecasts (ECMWF) Interim Reanalysis (ERA-Interim) [*Dee et al*., 2011], which uses a four-dimensional variational system and assimilates data from additional sources, performed better.

The present work expands upon the study of *Cox et al*. [2012], focusing on DLW over the GrIS. *Cox et al*. [2012] compared the DLW at Eureka, Nunavut, Canada (80°N, 86°W; 10 m), to the DLW at Barrow, Alaska (71°N, 156°W; 10 m), and found that these locations are characterized by a bimodal distribution in the DLW: one mode represents clear-sky conditions, while the other represents optically thick clouds. Intermediate DLW values that connect these maxima are associated with optically thin clouds, which have radiative characteristics that depend on their microphysical properties [*Cox et al*., 2014]. (This bimodal character of the Arctic atmosphere has also been described by other recent studies at Barrow and over the Arctic Ocean [*Stramler et al*., 2011; *Morrison et al*., 2012; *Pithan et al*., 2013].) *Cox et al*. [2012] then compared the results from the surface-based observations to the reanalysis data interpolated to the two locations to select a reanalysis product that best captured the DLW measured at each location. ERA-Interim, which exhibited the closest match to the bimodal distribution and the smallest biases in the DLW, was selected and used to provide spatial context to the results from Barrow and Eureka. Similar to *Shupe et al*. [2011], the results indicated that Eureka represents a region of the Arctic where cold, dry air from the north and off the GrIS supports a preponderance of clear-sky and thin clouds, as opposed to the frequent occurrence of thick clouds at Barrow, a location that receives moisture from a variety of directions.

In this study, we build upon the methodology of *Cox et al*. [2012] but focus on Summit, Greenland, and the GrIS. A new reanalysis evaluation is introduced that is more sophisticated than that used by *Cox et al*. [2012]. The present study has three main objectives. It first reports on observations of DLW measured at Summit from July 2010 through August 2012. The Summit DLW observations are then compared to reanalysis fields. Finally, these fields are used to analyze the spatial distribution of the influence of clouds on the DLW across the GrIS. To carry out these objectives, time-frequency decomposition (wavelet analysis) is used [*Torrence and Compo*, 1998]. Wavelet analysis is used to identify the significant time scales of variability in the DLW at

Summit and to compare the reanalysis fields to the surface-based observations using a method that is introduced in this study. The largely homogeneous surface over the central GrIS is ideal for comparing gridded ERA-Interim data to point data. The results of the analysis and evaluation are discussed together, providing mutually informative perspectives about the influence of clouds on the DLW over the GrIS.

The data sets are discussed in section 2. In section 3, the wavelet analysis and the evaluation technique are described. In section 4, the ERA-Interim DLW is considered in parallel with an analysis of the observations and a spatial analysis of the ERA-Interim data. Conclusions are presented in section 5.

2. Data

2.1. Surface-Based Observations

2.1.1. Atmospheric Emitted Radiance Interferometer

The atmospheric emitted radiance interferometer (AERI) is an infrared spectrometer that uses two reference blackbodies (one heated to a constant temperature and one ambient) for calibration; the overall radiance ($mW(m^2\,sr\,cm^{-1})^{-1}$) accuracy is better than 1% [*Knuteson et al*., 2004a, 2004b]. The spectral range is approximately 490 to 3000 cm^{-1} (achieved through the use of two detectors), and the spectral resolution is approximately 1 cm^{-1}. At Summit, the AERI was operated in rapid-sample mode, acquiring infrared radiances at subminute intervals at a zenith viewing angle. The raw data were processed partly using standard AERI processing routines [*Knuteson et al*., 2004b] and partly with slightly different routines developed by several of the authors [*Rowe et al*., 2011a, 2011b]. Quality control procedures screened for temperature instability in the reference sources, low instrument responsivity (used to identify frost-covered foreoptics), and excessive noise; these screenings removed 3.4% of the data. At Summit, the AERI viewport was located 2 to 3 m above the surface, depending on the level of drifting snow. During the first 7 months of the experiment, a hatch over the viewport was used to protect the instrument foreoptics during precipitation and blowing snow events, but the use of the hatch was discontinued because it actually increased the collection of snow in the foreoptics. About 1.7% (overall) of the data were removed because of hatch closures, with most of these occurring during 1 week in January 2011.

2.1.2. Downwelling Longwave All-Sky Flux, Clear-Sky Flux, and Cloud Radiative Forcing

The downwelling longwave all-sky flux (DLW_{allsky}) was derived using the AERI spectra, and the downwelling longwave clear-sky flux (DLW_{clrsky}) was calculated using vertical profiles of temperature and humidity, both using the method of *Cox et al*. [2012]. *Cox et al*. [2012] validated the method against a pyrgeometer at Barrow and reported that the uncertainty in the derived fluxes was 1–6 Wm^{-2}, with the largest uncertainties associated with optically thin clouds. This method includes simulating cloudy-sky radiances at multiple viewing angles as well as outside the spectral range of the AERI (i.e., 0 to 500 cm^{-1}) based on AERI zenith-view measurements and knowledge of the atmospheric state. The radiative transfer calculations of atmospheric gases were performed using the line-by-line radiative transfer model (LBLRTM) [*Clough and Iacono*, 1995; *Clough et al*., 1992], and cloudy-sky radiative transfer was performed using LBLDIS [*Turner*, 2005], which combines LBLRTM with emission and multiple scattering from cloud hydrometeors using the discrete ordinates radiative transfer (DISORT) algorithm [*Stamnes et al*., 1988]. (The acronym LBLDIS is a shortened form of LBLRTM-DISORT). Atmospheric profiles of temperature, pressure, and humidity used as input to the radiative transfer models were obtained from Vaisala RS-92 radiosondes that were launched twice daily at Summit by ICECAPS at 0 and 12 UTC. Trace gas profiles of O_3, N_2O, CO, and O_2 from the U.S. Standard Atmospheres [*McClatchey et al*., 1972] were also included in the simulations, as were NOAA's surface measurements of CO_2 [*Conway et al*., 2011] and CH_4 [*Dlugokencky et al*., 2010] made at Summit; the surface measurements were distributed through the profiles using a constant mixing ratio with height. Refer to *Cox et al*. [2012] for details of how the models and data are implemented for the radiative transfer calculations.

The DLW_{allsky} was calculated for 3 h averages of AERI spectra for the entire study period, and the DLW_{clrsky} was interpolated to the same temporal resolution following *Cox et al*. [2012]. This method also utilizes near-surface air temperatures, which were obtained by the NOAA Earth System Research Laboratory (ESRL) (archived at ftp://ftp.cmdl.noaa.gov/met/SUM/). This averaging time was chosen to be consistent with the reanalysis data set described in section 2.3.

The downwelling longwave contribution by clouds is calculated by subtracting the DLW_{clrsky} from the DLW_{allsky}. This parameter is referred to as downwelling longwave cloud radiative forcing ($DLW_{cldforce}$) and

was utilized previously in the Arctic by *Lesins et al*. [2009], *Mariani et al*. [2012], and *Cox et al*. [2012] and in the Antarctic by *Town et al*. [2005].

A continuous time series is important for the wavelet analysis used in this study. Approximately 5% of the AERI-derived DLW_{allsky} time series values are missing. These data gaps were filled using observations from a collocated Kipp and Zonen CG-4 pyrgeometer that is operated by the Steffen Research Group at the University of Colorado and the Cooperative Institute for Research in Environmental Sciences (CIRES). (This instrument is part of a suite of surface radiometers that are candidate instruments for the Baseline Surface Radiation Network (BSRN) [*Ohmura et al*., 1998].) We applied quality control procedures following the method of *Long and Shi* [2008], removing 0.7% of the data. This procedure includes climatological limits. The climatological limits for the BSRN site at Barrow, Alaska (71°N, 156°W; 10 m), used by *Long and Shi* [2008], were applied for Summit because Barrow is located close to the same latitude as Summit, but some of the minimum thresholds were lowered because Summit is colder than Barrow. The pyrgeometer data were averaged into 3 h periods to match the AERI DLW_{allsky}. The pyrgeometer observations were biased high compared to the AERI, primarily at low flux values, and this bias was positively correlated with solar elevation angle and scene (i.e., "cloudiness"). Because of this, a correction was applied to the pyrgeometer fluxes based on the AERI-derived fluxes [*Cox*, 2013]. Since no surrogate is available for data gaps in the radiosonde record, missing data in the DLW_{clrsky} were interpolated using a cubic spline.

The DLW_{allsky} derived from the AERI, the DLW_{clrsky} calculated from the radiosondes, and the associated $DLW_{cldforce}$ at Summit will be referred to as "surface-based observations" throughout the text.

2.3. ERA-Interim

The gridded reanalysis fields used here are from ERA-Interim [*Dee et al*., 2011]. ERA-Interim uses a four-dimensional variational assimilation system at 12 h intervals (0 and 12 UTC). ERA-Interim data were obtained from the ECMWF data archive (http://data-portal.ecmwf.int). The fields are on a 0.75° latitudinal/longitudinal grid. Each grid point represents a point location in space rather than an average of the area between the grid points (ERA-Interim Data frequently asked question: http://www.ecmwf.int/search/faqs).

ERA-Interim assimilates temperature and humidity profiles from radiosonde observations obtained via the Global Telecommunications System (GTS) for its reanalysis and forecast products. ICECAPS radiosondes were sent to the GTS, beginning in December 2011, but were not assimilated into ERA-Interim until December 2012 (P. Poli (ECMWF), personal communication, 2013). Therefore, ERA-Interim fields are independent of ICECAPS measurements during the entire study period.

Beginning from each analysis time, the ECMWF data assimilation system runs a forecast to the next analysis time. Radiative variables, such as DLW_{allsky}, are accumulated through time and reported every 3 h. To acquire 3 h mean DLW_{allsky} values, which are comparable to the DLW_{allsky} from the surface-based observations, the integrated energy ($W\,s\,m^{-2}$) is subtracted from the previous steps, and then the time duration is divided out (http://www.ecmwf.int/search/faqs).

DLW_{clrsky} is not directly available from the ECMWF data server. Using the notation LW for net longwave and ULW for upwelling longwave, DLW_{clrsky} was obtained from existing fields LW_{clrsky}, LW_{allsky}, and DLW_{allsky}, as follows: $DLW_{clrsky} = LW_{clrsky} - ULW_{clrsky}$. Further, ULW_{clrsky} is assumed to be equal to ULW_{allsky}. This corresponds to assuming a surface infrared reflectivity from clouds of 0, which results in an error of about 1% in $DLW_{cldforce}$. Finally, ULW_{allsky} is calculated from $LW_{allsky} - DLW_{allsky}$.

Another source of uncertainty in estimating DLW_{clrsky} comes from ECMWF's estimate of LW_{clrsky}. A comparison between LW_{clrsky} and LW_{allsky} during times when ERA-Interim did not include clouds (total cloud cover = 0) revealed a difference of $0.4 \pm 1.2\,Wm^{-2}$.

$DLW_{cldforce}$ is calculated as $DLW_{allsky} - DLW_{clrsky}$ and thus has the uncertainties inherent in DLW_{clrsky} described above.

The ERA-Interim elevation model (0.75° grid) reaches a maximum of 3172.6 m over the GrIS and is 3165.7 m when interpolated to the Summit coordinates. This places the altitude for ERA-Interim at the latitude and longitude of Summit roughly 44 m below the actual elevation of the station above mean sea level (3209.5 m; http://summitcamp.org), adding to the path length of the lower atmosphere in the radiative transfer calculation for the ERA-Interim radiation fields. Additionally, strong, shallow, and persistent surface-based

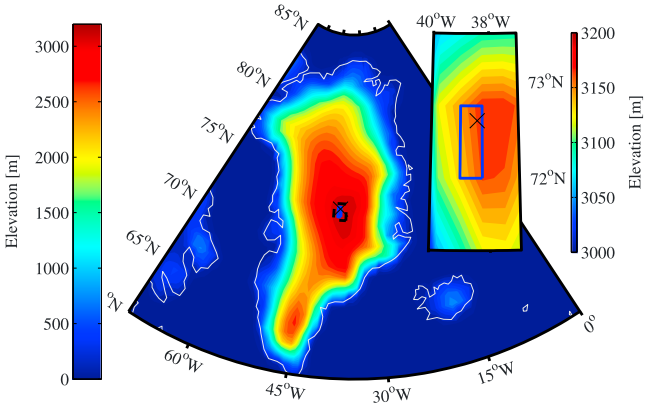

Figure 1. Map of Greenland and vicinity. The contours show elevation from ERA-Interim. The contour intervals are 100 m for the large map and 10 m for the inset map. The blue box illustrates the ERA-Interim grid box surrounding Summit Station, which is denoted by the X.

temperature inversions at Summit [*Shupe et al.*, 2013; *Miller et al.*, 2013a] are poorly resolved by the model, which results in higher near-surface air temperatures compared to ICECAPS radiosondes [*Miller et al.*, 2013b].

Figure 1 shows an elevation contour map of Greenland from ERA-Interim. The ERA-Interim grid was interpolated to Summit using bilinear interpolation.

3. Wavelet Analysis Methodology

Wavelet analysis is a time-frequency decomposition technique. Using a wavelet transform, time-dependent power (variance) can be estimated, allowing not only identification of the time scales of variability but also the variations in the time scales as a function of time. This work uses wavelet analysis to determine the significant time scales of variability in DLW_{allsky} at Summit and to compare variability in the surface-based observations of DLW_{allsky} and DLW_{clrsky} at Summit to that from ERA-Interim. The continuous wavelet transform is used. Details of the methodology as applied here are discussed below, including assessing statistical significance of the variability and uncertainty in the variance comparisons.

3.1. Determining Time Scales of Variability

Torrence and Compo [1998, section 7] outline seven steps for wavelet analysis using a discrete approximation to the continuous wavelet transform. First, the Fourier transform of the discrete time series (x_n, where n is the time index) is computed. Here two time series are used: the DLW_{clrsky} and the DLW_{allsky}. The time series are zero padded before the Fourier transform is performed (yielding $\hat{x}_k$, where k is the frequency index). In the second and third steps, the wavelet function and set of scales (s), which describe the width of the wavelet in time, are chosen, and the normalized wavelet function [$\psi(s,\omega)$] is created for each s, as a function of angular frequency ω. In this work, scales from 0.25 (the smallest resolved period of 3 hourly averages) to 365 days are used. A variety of wavelet bases were tested, some that provide more time precision and less frequency precision, and some the opposite, and it was found that the results were qualitatively similar. The needs of this study required more frequency precision since we focus in part on relatively large, continuous blocks of time (seasons, for example). Wavelets that enhance the information content in the time domain tend to smooth out the scale-dependent features that are of interest here. The Morlet wavelet was selected for analysis. The normalized Morlet wavelet is

$$\psi(s,\omega) = \left(\frac{2\pi s}{\delta t}\right)^{1/2} \pi^{-1/4} H(\omega) \exp\left[-(s\omega - \omega_0)^2/2\right], \quad (1)$$

where δt is the time step and H is the Heaviside step function. For the Morlet wavelet, the nondimensional frequency (ω_0) is set to 6, satisfying admissibility [*Farge*, 1992] and ensuring that s is very closely related to the Fourier period in traditional Fourier spectral analysis [*Meyers et al.*, 1993]; therefore, small scales represent high frequencies (shorter periods), and large scales represent low frequencies (longer periods). In this work, all scales are converted to the equivalent Fourier period.

In step 4, the wavelet transform is calculated according to

$$W_n(s) = \sum_{k=0}^{N-1} \hat{x}_k \psi^*(s\omega_k) \exp(i\omega_k n \delta t), \quad (2)$$

where the parentheses represent functionality and the asterisk represents the complex conjugate. Wavelet power, $|W_n(s)|^2$ [*Torrence and Compo*, 1998], will be referred to simply as "power" in the text.

The times series used here were zero padded; convolution of the zero-padded time series with the wavelet function (or multiplication in the frequency domain, as in equation (1)) weakens the signals near the edges of the time series, extending them into the zero-padded region. Step 5 involves determination of this affected region, termed the cone of influence (COI). The COI used here is a function of scale and follows that of *Torrence and Compo* [1998]. Here we take this a step further and attempt to calculate the error in the variance as a function of scale. Additionally, to investigate the sensitivity to our choice of edge treatment, we compared the results using a time series that cuts off 24 months after the beginning date (thus, assuming the entire time series is periodic and padding is unnecessary). We found little sensitivity to the results using these different edge treatments.

Step 6 is to plot the wavelet power spectrum as contours, as a function of time and period (corresponding to s), to identify modes of variability.

The seventh step is to determine the 2.5% and 97.5% significance contours. Here the statistical significance of the wavelet power is determined by comparing to a red noise background power spectrum, following *Torrence and Compo* [1998], and is used to quantify the significant time scales of variability of the surface-based observations (section 4.1.2).

An additional step that can be included is to reconstruct the time series from the wavelet-transformed data. This is useful as a diagnostic and enables creation of time series including only certain scales.

3.2. Variance of a Reconstructed Time Series

Using an inverse wavelet filter, the original time series can be reconstructed from the transform or partially reconstructed over scales of interest [*Farge*, 1992; *Torrence and Compo*, 1998]. Since the wavelet transform used here is continuous, this reconstruction can be performed using a delta function [*Farge*, 1992] and is given by *Torrence and Compo* [1998] as

$$x_n' = \frac{\delta j \delta t^{1/2}}{C_\delta \psi_0(0)} \sum_{j=j_1}^{j_2} \frac{\Re\{W_n(s_j)\}}{s_j^{1/2}}, \tag{3}$$

where the time series is reconstructed over the scale from s at index j_1 through j_2 (where the js are defined such that $s_j \equiv s_0\, 2^{j\delta j}$), C_δ is a wavelet-specific parameter, δj is a parameter associated with the iteration through s, and $\psi_0(0)$ accounts for energy scaling. The values for these parameters were set for a Morlet wavelet ($\omega_0 = 6$) as recommended by *Torrence and Compo* [1998] in their Table 2.

Following *Torrence and Compo* [1998], the variance of equation (3) can be reconstructed as

$$\sigma_M^2 = \frac{\delta j\ \delta t}{C_\delta N} \sum_{n=0}^{M-1} \sum_{j=j_1}^{j_2} \frac{|W_n(s_j)|^2}{s_j}, \tag{4}$$

where N is the length of the original time series. If M is set to N, then equation (4) gives the variance of the reconstructed time series within the original bounds. Defining variance as a function of scale,

$$\sigma_{j,M}^2 = \frac{\delta j\ \delta t}{C_\delta N} \sum_{n=0}^{M-1} \frac{|W_n(s)|^2}{s_j}, \tag{5}$$

allows for the calculation of the variance spread into the zero-padded region, which depends on s_j, and can be large when s_j is large compared to the length of the time series. The dispersed variance can be estimated by computing equation (5) twice, with M set alternatively to N and to the length of the zero-padded times series, N_p,

$$\rho_j^2 = \sigma_{j,N_p}^2 - \sigma_{j,N}^2. \tag{6}$$

For the DLW_{allsky} (DLW_{clrsky}) time series used in this study, about 16% (22%) of the variance was distributed outside of the original bounds of the time series; most of this dispersed variance (2/3) corresponds to variation from the seasonal cycle, which has a period roughly half the length of the time series.

The continuous wavelet transform results in better scale representation and a smoothly varying transform but also includes redundant information, which introduces a small amount of error into the reconstruction,

even outside the COI. *Torrence and Compo* [1998] suggest ensuring that this error is small. The error, ε^2, associated with the reconstruction, is found as follows:

$$\varepsilon^2 = \mathrm{var}(x_n) - \sigma_{N_p}^2. \tag{7}$$

Note that we use N_p here to avoid including ρ^2 in the calculation of ε^2. The reconstruction error (equation (7)) is <1.4% of var(x_n) for each of the time series used in this study. Unlike the error in the COI, ε is assumed to be relatively scale-independent and proportional to variance:

$$\varepsilon_j^2 = \varepsilon^2 \frac{\sigma_{j,N_p}^2}{\sigma_{N_p}^2}. \tag{8}$$

By combining equations (5), (6), and (8), the variance of the reconstructed time series, as a function of scale (represented by *j*), is related to the variance of the original time series, x_n, by

$$\sum_{j=0}^{J} \sigma_{j,N}^2 + \varepsilon_j^2 + \rho_j^2 = \mathrm{var}(x_n). \tag{9}$$

3.3. Difference in Variance Between Two Reconstructed Time Series

Using equation (9), the difference in variance between two time series, a_n (ERA-interim) and b_n (surface-based observations), as a function of scale index *j*, can be represented as follows:

$$\Delta\sigma_j^2 = \left[\Delta\sigma_{j,N}^2(a) - \Delta\sigma_{j,N}^2(b)\right] + \left[\Delta\varepsilon_j^2(a) - \Delta\varepsilon_j^2(b)\right] + \left[\Delta\rho_j^2(a) - \Delta\rho_j^2(b)\right]. \tag{10}$$

To help understand equation (10), note that the total variance, over all scales, can be determined by summing equation (10) over *j*. This is then comparable to the difference in variances between the original time series:

$$\sum_{j=0}^{J} \Delta\sigma_j^2 = \mathrm{var}(a_n) - \mathrm{var}(b_n). \tag{11}$$

Note that equation (11) expresses a net difference because $\Delta\sigma_j^2$ may include compensatory differences (it may be positive at some *j* and negative at others), and therefore, the total difference can be found by summing over the absolute value of $\Delta\sigma_j^2$, which will be greater than or equal to var(a_n) − var(b_n).

3.4. Use of Wavelets in Reanalysis Evaluation

The primary diagnostic tool used for the reanalysis evaluation in this manuscript is to compare the partial time series reconstruction (equation (3)) and the scale-dependent variance (equation (5)) between two data sets (i.e., the surface-based observations and ERA-Interim) that independently estimate the same parameter (i.e., DLW) at the same temporal resolution (i.e., 3 h averages). Comparisons are made in section 4.2.2 using two metrics, the squared correlation coefficient r^2 of the reconstruction x'_n (equation (3)) and the scale-dependent variance difference $\Delta\sigma_j^2$ (equation (10)). The values for the residual dispersed variance ($\Delta\rho_j$) and the reconstruction error ($\Delta\varepsilon^2$) are used to estimate uncertainty in the difference in variance. We also include an estimate of the fraction in time of $\Delta\sigma_j^2$ that is under the COI when displaying results.

Statistical methods have been developed to identify significance in wavelet power relative to a specified null hypothesis (indicating no statistical significance) [*Torrence and Compo*, 1998]. Statistical significance is not applied in the evaluation. Instead, uncertainty is used (equations (6) and (7)) because wavelet parameters and edge treatments are identical, so the differences between the time series are an accurate measure within this uncertainty. Statistical significance against a discrete univariate lag-1 autoregressive red noise background [*Torrence and Compo*, 1998, equation (16)] is applied to identify the significant time scales of variability from the surface-based observations (section 4.1.2).

4. Results and Discussion

4.1. Downwelling Longwave Flux at Summit Station

In this section, the DLW at Summit is presented and discussed. In section 4.1.1, the distributions of the observed DLW at Summit are analyzed and compared to ERA-Interim. The reasons for the differences between the

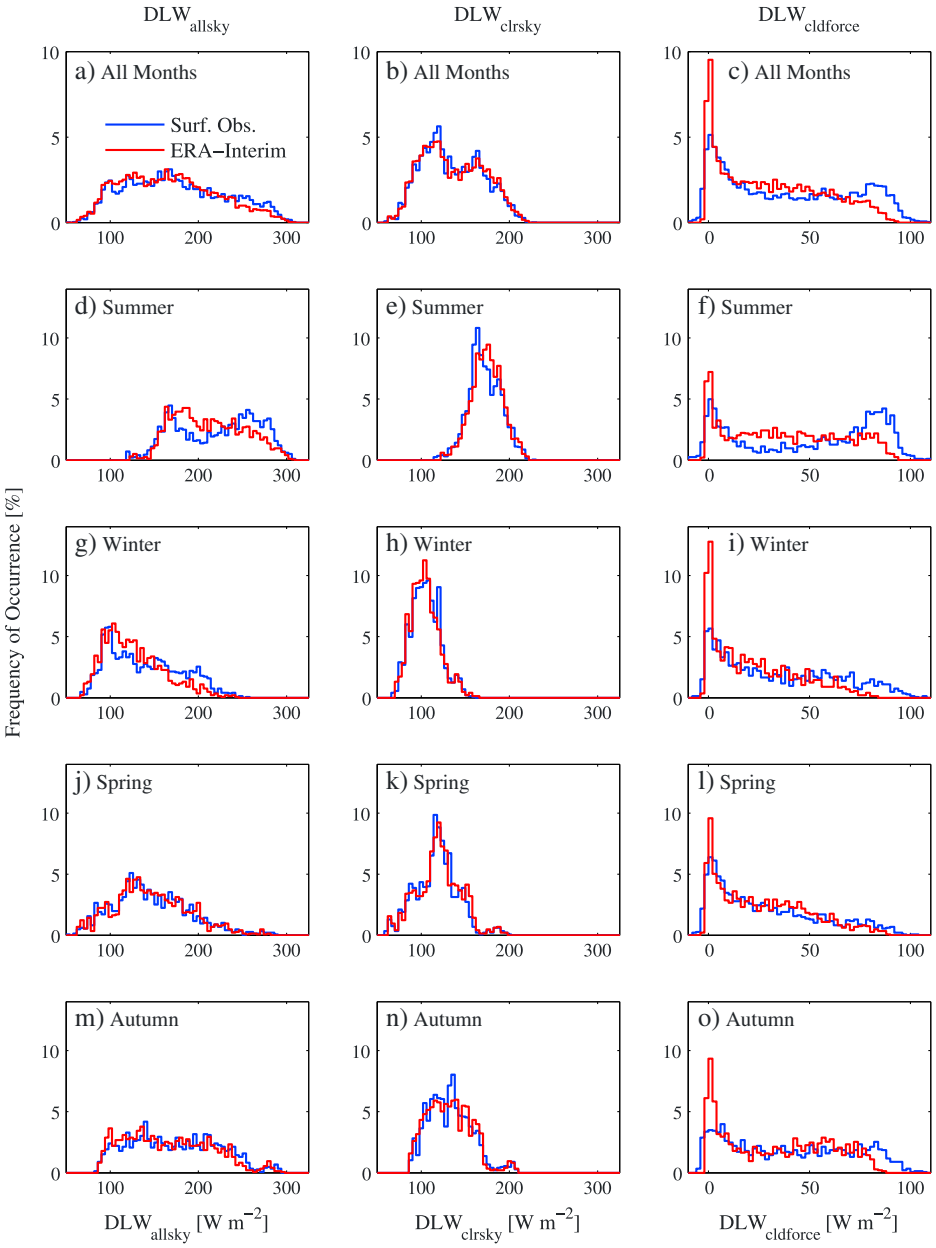

Figure 2. Histograms of the 3 h temporal resolution fluxes at Summit Station from surface-based observations (blue) and ERA-Interim (red). (a, d, g, j, and m) The downwelling longwave all-sky flux (DLW_{allsky}). (b, e, h, k, and n) The downwelling longwave clear-sky flux (DLW_{clrsky}). (c, f, i, l, and o) The downwelling longwave cloud radiative forcing ($DLW_{cldforce}$). The bin size is 4 W m^{-2} for DLW_{allsky} and DLW_{clrsky} and is 2 W m^{-2} for $DLW_{cldforce}$. Figures 2a–2c are for all data, followed by the following seasons: (Figures 2d–2f) summer (JJA), (Figures 2g–2i) winter (DJF), (Figures 2j–2l) spring (MAM), and (Figures 2m–2o) autumn (SON).

surface-based observations and ERA-Interim are investigated. In section 4.1.2, the wavelet transform (equation (1)) is used to identify significant time scales of variability in DLW_{allsky} at Summit.

4.1.1. Distributions of DLW

Figure 2 shows the probability density functions (PDFs) of 3 hourly DLW_{allsky}, DLW_{clrsky}, and $DLW_{cldforce}$ at Summit from surface-based observations and the ERA-Interim data set for all months, summer (June-July-August (JJA)), winter (December-January-February (DJF)), spring (March-April-May (MAM)), and autumn (September-October-November (SON)). Means, variances, differences in the means and variances, and squared correlation coefficients are provided in Table 1. Also provided in Table 1 are the results of one-sample

Table 1. Surface Observations and ERA-Interim Comparison: Summary Statistics[a]

	Surface Observations		ERA-Interim		Difference: ERA-Interim − Surface Observations				
	Mean (Wm^{-2})	Var. $(Wm^{-2})^2$	Mean (Wm^{-2})	Var. $(Wm^{-2})^2$	r^2	ME (Wm^{-2})	σ (Wm^{-2})	K–S D_{ks} (p)	t Statistics (p)
DLW_{allsky}	174.2	3149.3	166.6	2769.5	0.8	−7.5	24.9	**0.0605 (<0.01)**	**24.1 (<0.01)**
Summer (JJA)	221.3	2081.3	211.9	1565.7	0.59	−9.4	29.6	**0.1565 (<0.01)**	**14.14 (<0.01)**
Winter (DJF)	139.8	1706	126.8	1157.3	0.74	−13	21.2	**0.172 (<0.01)**	**23.38 (<0.01)**
Autumn (SON)	172.7	2399.1	165.3	2297.4	0.77	−7.4	24	**0.0694 (<0.01)**	**11.75 (<0.01)**
Spring (MAM)	146.5	1842.3	146.7	1737.2	0.79	0.2	20.2	0.0245 (0.766)	0.333 (0.739)
DLW_{clrsky}	135.7	1125.7	136.1	1188.5	0.97	0.9	5.6	**0.0285 (0.011)**	**12.78 (<0.01)**
Summer (JJA)	171.9	341.4	174.4	312.4	0.89	2.47	6.1	**0.0991 (<0.01)**	**18.02 (<0.01)**
Winter (DJF)	105.5	271.3	104.6	268.3	0.93	−0.86	4.27	**0.0552 (0.023)**	**7.625 (<0.01)**
Autumn (SON)	132.4	584.9	132	623.4	0.94	−0.47	6.2	0.0337 (0.376)	**2.879 (<0.01)**
Spring (MAM)	118	574.8	119.9	609.1	0.97	1.87	4.58	**0.0543 (0.025)**	**15.66 (<0.01)**
$DLW_{cldforce}$	39	989	30.6	660.3	0.46	−8.4	23.6	**0.1482 (<0.01)**	**28.55 (<0.01)**
Summer (JJA)	49.4	1187.6	37.5	780.8	0.38	−11.9	28	**0.2398 (<0.01)**	**18.85 (<0.01)**
Winter (DJF)	34.3	829.6	22.2	448.1	0.49	−12.1	20.5	**0.1954 (<0.01)**	**22.53 (<0.01)**
Autumn (SON)	40.3	912	33.4	701.3	0.48	−6.9	22.5	**0.1257 (<0.01)**	**11.71 (<0.01)**
Spring (MAM)	28.5	680.3	26.8	513.7	0.51	−1.69	18.6	**0.0632 (<0.01)**	**3.481 (<0.01)**

[a]Summary statistics for the comparison between ERA-Interim longwave fluxes interpolated to Summit and the surface-based observations measured at Summit from July 2010 through August 2012. DLW_{allsky} is the downwelling longwave all-sky flux, DLW_{clrsky} is the downwelling longwave clear-sky flux, and $DLW_{cldforce}$ is the downwelling longwave cloud radiative forcing. ME = mean error, σ = standard deviation. Negative ME means ERA-Interim biased low relative to the surface-based observations. K–S is the two-sample Kolmogorov–Smirnov statistics, D_{ks}; the t test is a one-sample test for ERA-Interim minus surface-based observations differences against the null hypothesis that the mean = 0. Statistically significant results at the 5% significance level are highlighted in bold, and P values are shown in parentheses.

Student's t tests for the mean of the differences in the PDFs against a null hypothesis of 0 (the differences are assumed to be normally distributed). The t test results indicate that the biases between the observed and ERA-Interim distributions in Figure 2 are statistically significant (P values <0.05, indicating very low likelihood that the biases could occur by chance) with the exception of the DLW_{allsky} in spring (P value of 0.7) and the DLW_{clrsky} in autumn (P value of 0.4). Results from two-sample Kolmogorov–Smirnov (D_{ks}) tests are also provided. The D_{ks} indicates the differences in the distributions that can arise from differences in means, variances, median, or shape of the PDFs and is a nonparametric test that makes no assumptions about the shape of the distributions.

The shape of the PDF of DLW_{allsky} (Figure 2a) appears to be reasonably well matched by ERA-Interim, with a single mode near 155 W m^{-2} and a skew toward higher values. However, ERA-Interim has slightly more values near the mode and fewer at high values, and therefore, the PDFs are different statistically ($D_{ks} = 0.0605$). The similarity of the shape of the PDFs is qualitatively comparable to that previously seen between ERA-Interim and observed DLW_{allsky} at Barrow and Eureka [*Cox et al.*, 2012], but the DLW_{allsky} PDF shown here is shifted to lower fluxes by about 50 W m^{-2} compared to those locations. Furthermore, the DLW_{allsky} at Barrow and Eureka were bimodal; of the two modes, there was a larger peak corresponding to clear sky and optically thin clouds at Eureka and a larger peak corresponding to optically thick clouds at Barrow [*Cox et al.*, 2012, Figure 9]. At Summit, there is a suggestion of a small second maxima at ~250 W m^{-2}, but overall one broad mode is apparent. Thus, Summit represents a third typology with a single mode in DLW_{allsky}. The surface-based observations exhibit a bimodal distribution in summer (Figure 2d); this characteristic is not represented by ERA-Interim. In other seasons (Figures 2g, 2j, and 2m), DLW_{allsky} is not bimodal, and ERA-Interim better captures the PDF shapes.

The comparison between ERA-Interim DLW_{clrsky} and surface-based observations is shown in Figure 2b. Qualitatively, this distribution is well represented by ERA-Interim, but like DLW_{allsky}, it is different statistically from the surface-based observations at the 5% significance level ($D_{ks} = 0.0285$). The PDF is bimodal with a summer mode at higher values and a winter mode at lower values (the seasonal separation can be seen by comparing Figures 2e and 2h). Similar to the findings at Eureka of *Cox et al.* [2012] (for temperature and humidity) and *Cox et al.* [2014] (for cloud ice fractions and optical depths), this likely represents two distinct states in the Summit meteorology that are separated due to a very strong annual cycle. The mean difference (bias) between ERA-Interim DLW_{clrsky} and surface-based observations is small (Table 1), especially considering the limitations of the ERA-Interim elevation model and near-surface air temperatures noted earlier (see section 2.3).

Despite the statistically significant biases in ERA-Interim DLW_{clrsky} distributions, the statistics in Table 1 indicate that the representation of DLW_{clrsky} in ERA-Interim is considerably better than for the DLW_{allsky}: DLW_{clrsky} is better correlated with surface-based observations and has lower mean bias and standard deviation (Table 1). Thus, the differences between the surface-based observations and ERA-Interim DLW_{allsky} are primarily associated with the representation of clouds. Comparing the $DLW_{cldforce}$ highlights these differences (Figure 2c). Unlike the DLW_{allsky}, the $DLW_{cldforce}$ distribution derived from the surface-based observations is bimodal. Clear-sky conditions form a peak around zero (within the uncertainty of the measurement); a second peak appearing that is likely due to warmer, thicker clouds, and intermediate values is likely associated with either optically thin clouds, which have much more variable radiative characteristics [*Turner*, 2005; *Stramler et al*., 2011; *Cox et al*., 2012, 2014], or a mixture of clear and cloudy periods averaged together over the 3 h period. (See *Cox et al*. [2014] for a discussion of the relationship between cloud optical thickness and $DLW_{cldforce}$.) *Stramler et al*. [2011] refer to this bimodal nature of the Arctic atmosphere as radiatively clear and opaquely cloudy. However, note that for this time period at Summit, the frequency of clouds between the radiatively clear and opaquely cloudy states is large compared to the frequencies at the two modes, especially in winter, spring, and autumn (Figures 2i, 2l, and 2o), suggesting that there are many cases that fall in between radiatively clear and opaquely cloudy states. This implies that the intermediate state is not necessarily representative of a transition state at Summit, as was postulated by *Stramler et al*. [2011] for winter clouds over the Arctic Ocean. In fact, the Summit summer most closely represents the winter states described by *Stramler et al*. [2011]. This is likely due to the generally colder and drier conditions at Summit relative to lower altitude locations in closer proximity to the Arctic Ocean, which may limit the occurrence of the thickest clouds. The opaquely cloudy mode in $DLW_{cldforce}$ is not present in winter or spring, although some opaquely cloudy cases do exist (Figures 2i and 2l). ERA-Interim includes a larger frequency of intermediate and low $DLW_{cldforce}$ values, particularly for clear states ($DLW_{cldforce}$ near 0 W m^{-2}), and a smaller frequency of large $DLW_{cldforce}$ values, compared to the surface-based observations. Thus, the mean $DLW_{cldforce}$ is smaller in ERA-Interim, which also explains the low bias in the DLW_{allsky} (Table 1). The overestimation of the frequency of thin clouds occurs primarily in summer when the surface-based observations more clearly exhibit the radiatively clear and opaquely cloudy states. ERA-Interim does not show the opaquely cloudy mode in summer (Figure 2f). ERA-Interim represents the $DLW_{cldforce}$ best in spring, possibly due to a relative lack of thick clouds. In winter and autumn, ERA-Interim has few clouds with $DLW_{cldforce} > 80$ W m^{-2} (the thickest clouds), but the surface-based observations indicate many clouds with $DLW_{cldforce} > 80$ W m^{-2}. In all seasons, especially winter and autumn, ERA-Interim has more clear states (~0 W m^{-2}) than the surface-based observations.

4.1.2. Significant Time Scales of Variability

The significant time scales of variability in DLW_{allsky} at Summit are investigated in this section. They comprise a substantial portion of the observed variance spectrum compared to the distribution expected from red noise (see section 3.4).

Figure 3a shows the wavelet power spectrum of anomalies of DLW_{allsky} from surface-based observations (scales 0.25–128 days). Regions with power that are significant at the 95% confidence level are outlined in black, indicating the time scales of variability that have amplitudes that are significantly larger than expected from red noise. These regions may indicate time scales over which transitions between clear and cloudy states occur or transitions between relatively warm and moist and cold and dry air masses. Note that since the time series in this study are relatively short, statistically significant features may still represent stochastic fluctuations and not have climatological significance. Anomalies are used because variability at large periods is associated with the seasonal cycle. The anomaly time series were created by subtracting a least squares fit to the first three harmonics of the seasonal cycle. This is necessary for statistical testing against the null hypothesis of red noise. Since the time series is relatively short, the properties of the seasonal cycle are not well defined. This may cause some uncertainty in the statistical testing but does not affect the wavelet transform because the high-frequency variability is independent of the first three harmonics.

As seen in Figure 3a, low-frequency (> ~32 days) variability is significant from the late autumn through early spring in both years. Higher-frequency (16–32 days) variability is important during much of the year but not late summer. There is relatively little significant variability between periods of 6 and 12 days throughout the record, indicating that at these time scales, variability is consistent with what is expected from red noise.

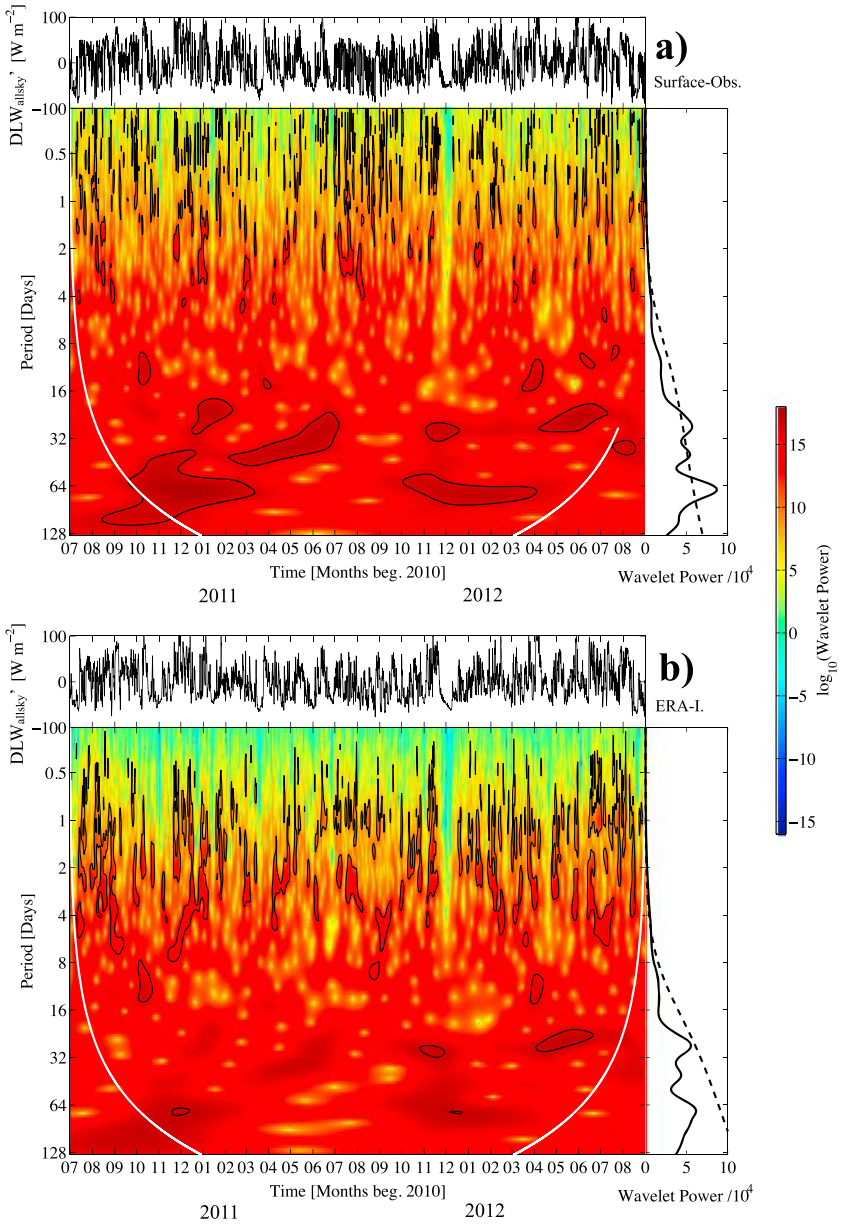

Figure 3. (a) The wavelet power spectrum of the downwelling longwave all-sky flux (DLW_{allsky}') anomalies from the surface-based observations for periods between 0.25 and 128 days (center). The prime indicates that the time series is an anomaly. (b) Similar to Figure 3a but for DLW_{allsky}' anomalies from ERA-Interim. The first three harmonics were removed from the time series (Figures 3a and 3b, top) to compute anomalies before the wavelet transform was performed. The time-averaged wavelet power spectrum is shown in the panel to the right; the dashed line indicates the 95% significance level. The white curves show the cone of influence; below this line edge effects are important. The dark red contours indicate high power, and the blue contours indicate low power; high power significant to the 95% level is marked by black contours. The color scale is the $\log_{10}$ of the wavelet power and has the same limits in both Figures 3a and 3b.

A qualitatively similar figure is produced when the ERA-Interim time series is transformed (Figure 3b). The main difference between Figures 3a and 3b is the regions of the power spectrum identified as significant. For ERA-Interim, statistically significant variability is mostly between periods of 0.5 and 4 days. This is due to differences in the lag-1 autocorrelation of the two time series, which was used to determine the red noise process. The autocorrelation functions of the anomaly time series are discussed in section 4.2.1.

Some of the most interesting features that appear in Figure 3 are the extended clear-sky periods that occur throughout the year (e.g., December 2011). These features appear as vertically elongated regions of low

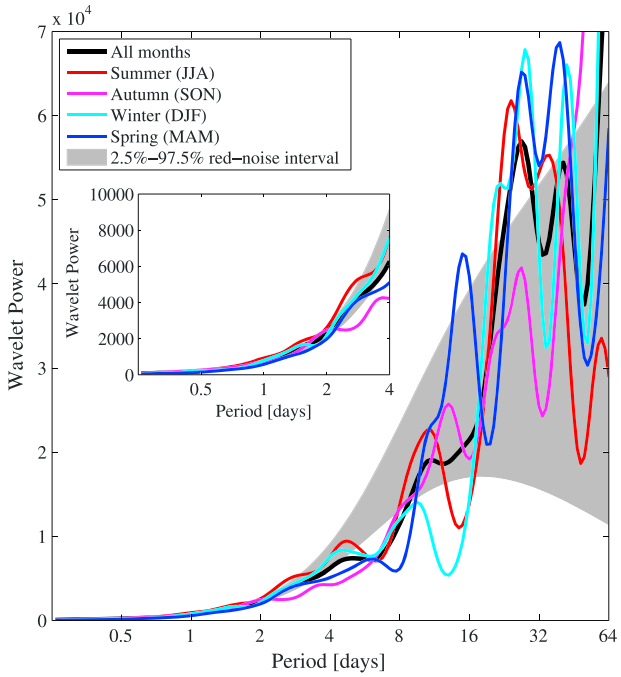

Figure 4. Average power spectra for the downwelling longwave all sky-flux (DLW_{allsky}) from the surface-based observations computed using the wavelet transform. Periods between 0.25 and 64 days are shown. A 95% confidence interval (2.5% to 97.5%) is shown in gray (see text for details). The inset shows an expanded view of periods smaller than 4 days.

power. They are characterized by a lack of power at time scales with periods smaller than the duration of the event, which suggests that clouds (even thin clouds) are not present during these times. The period of these features is similar to the duration of the event (the Morlet wavelet provides similar precision in both the time and frequency domains); for example, in December 2011, the clear-sky time lasted approximately 10 days, and the low-power region extends from the periods of 0.25 to 8 days. These features typically last from 1 day to 1 week and are generally well represented by ERA-Interim. In contrast to low-power features, which are found at relatively high-frequency variability, high-power, significant features (black contours) are evident at many time scales. These are more likely to be associated with clouds because there is a high variability in DLW_{allsky} during cloudy times and during transitions between clear and cloudy skies.

Figure 4 shows the time-averaged power spectra from surface-based observations of DLW_{allsky} for each of the four seasons (JJA, SON, DJF, and MAM) and for the whole time series. (The black line in the figure, representing all months, is the same as the average power spectrum in Figure 3a (right).) A 2.5%–97.5% confidence interval about the red noise spectrum based on the overall time series is also shown as a gray-shaded region (power should be interpreted as significant compared to the overall time series when it extends above or below the gray-shaded region, but note that the confidence interval differs from the significance level shown in Figure 3). Power is significantly lower than expected (i.e., lower than for red noise) for periods of 5 to 8 days for all months, but the range of the periods corresponding to this deviation varies with season. The smallest ranges occur for the transition seasons: autumn (2–8 days) and spring (4–9 days), while the largest ranges occur during winter (5–17 days) and summer (5–8 and 12–18 days). Each of the seasons has a peak in power in the 10 to 14 day time scale (note that these peaks are not statistically significant at the 95% confidence interval except in spring); slight differences in the time scale of these peaks and relatively large differences in the magnitudes of the power may suggest seasonality. In spring, most of the short-term high power is encompassed in a prominent 14 day period. High power in all seasons except autumn occurs between periods of 21 to 28 days. Summer is the only season with a significant peak near the synoptic scale, at approximately 3 days.

4.2. ERA-Interim Evaluation

In this section, the DLW from ERA-Interim is evaluated using wavelet analysis as described in section 3 and using other statistics. In section 4.2.1, the autocorrelation functions of the two DLW_{allsky} time series are compared to set an expectation for the spatial-temporal relationship between the point observations and the gridded data. In section 4.2.2, the evaluation using wavelet analysis is presented.

4.2.1. Autocorrelation Functions

Autocorrelation functions represent system "memory"; that is, the amount by which the system state at time t_0 influences a subsequent time $t_0 + \tau$. To highlight the differences between the DLW_{allsky} estimates from ERA-Interim and the surface-based observations, Figure 5 shows the autocorrelation function for the lags from 0.125 days to 6 days—48 total lags—for both the anomaly time series of surface-based observations and ERA-Interim (recall that the ERA-Interim data are linearly interpolated to Summit). Again, the first three harmonics of the seasonal cycle were removed from each time series to construct anomalies that emphasize weather-related variability.

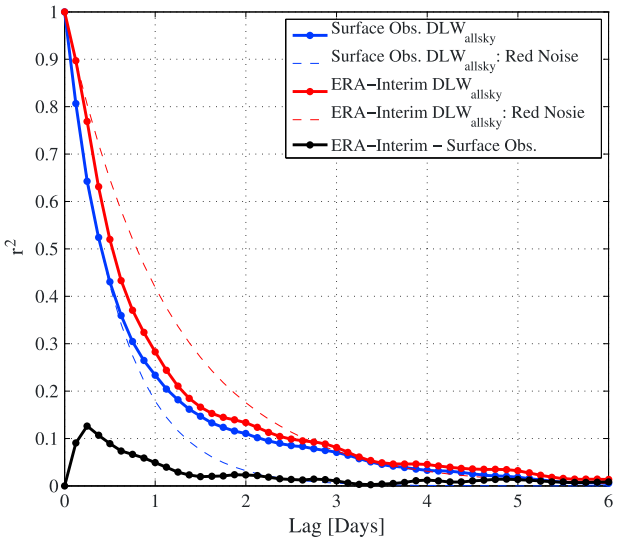

Figure 5. Autocorrelation functions as a function of lag from the downwelling longwave all-sky flux (DLW_{allsky}) time series (8 times daily) plotted for lags out to 6 days (48 lags) for the surface-based observations (blue) and ERA-Interim (red). For each time series, the first three harmonics of the seasonal cycle were removed before the autocorrelation function was calculated. The dashed lines show the expected autoregressive red nose calculated from the lag-1 autocorrelation coefficient, which is estimated by combining the sample lag-1 (α_1) and the lag-2 (α_2) coefficients following *Torrence and Compo* [1998] as $(\alpha_1 + \sqrt{\alpha_2})/2$. The black line shows the difference between the autocorrelation functions (ERA-Interim minus surface-based observations).

Autocorrelation drops off at a rate consistent with red noise in the surface-based observations for approximately the first 4 lags (0.5 days) before persisting above expected lag-1 autoregressive red noise. For lags of less than 3 days, the memory in the ERA-Interim data is retained longer than the surface-based observations, but less than the red noise expectation from its lag-1 autocorrelation (dashed line), and it only persists above red noise after the 3 day lag time. The ERA-Interim autocorrelation function converges with the surface-based observations at lags between 2 and 4 days before diverging slightly again. Recall that differences in the lag-1 autocorrelation are responsible for the differences in red noise background spectra that were used to identify statistical significance in Figures 3a and 3b.

The increased memory in ERA-Interim over short time periods compared to the surface-based observations may be associated with the coarse spatial footprint that cannot resolve local variability and therefore is primarily influenced by larger scale, more slowly varying time scales. For example, a horizontal transect across the ERA-Interim 0.75° grid pixel is on the order of 100 km. If the surface wind speed is assumed to be between 1 m s^{-1} and 15 m s^{-1} [*Shupe et al.*, 2013], then the time for a parcel of air to cross the pixel is between 2 to 28 h, or roughly on the order of 0.5 days. This corresponds approximately to the lag time of the peak in the differences between ERA-Interim and the surface-based observations at ~0.5 days (black line in Figure 5).

4.2.2. Wavelet-Based Comparison

Figure 3 showed that the wavelet power spectra of the DLW_{allsky} from ERA-Interim and the surface-based observations were qualitatively similar. However, the variance of the ERA-Interim DLW_{allsky} time series is ~12% less than the observed DLW_{allsky} (Table 1). To determine the time scales that contribute to this difference (that is to quantify the differences between Figures 3a and 3b), we use the wavelet analysis described in section 3. As ERA-Interim and the surface-based observations represent the same realization of the signal, differences at all time scales are important, regardless of whether or not the time scales are statistically significant compared to the null hypothesis.

The wavelet-based comparison between ERA-Interim and the observed fluxes is shown in Figure 6. All 26 months of the study period are included in Figure 6a. Figures 6b–6e show the results for individual seasons. Anomalies are not used here because statistical significance against red noise is not applied. The seasons are classified into 3 month groups (as in Figure 4) so that the relative magnitudes of the time scale-dependent reconstructed variance, $\Delta\sigma_j^2$, can be more easily compared. Note that three Julys and three Augusts are represented in the 26 month time series, but only two each for all additional months; therefore, a disproportionately large amount of the total variance from Figure 6a is contained in Figure 6b compared to Figures 6c–6e. Recall from equation (11) that the sum over all $\Delta\sigma_j^2$ is equal to the difference in variance between the two original time series. Figure 6 shows that there are compensatory biases in $\Delta\sigma_j^2$ so that the net variance difference between the time series underestimates the actual differences between the time series. The integrated variance differences (summing over the absolute value in equation (11)) are actually about 25% greater for DLW_{allsky} and 87% greater for DLW_{clrsky}.

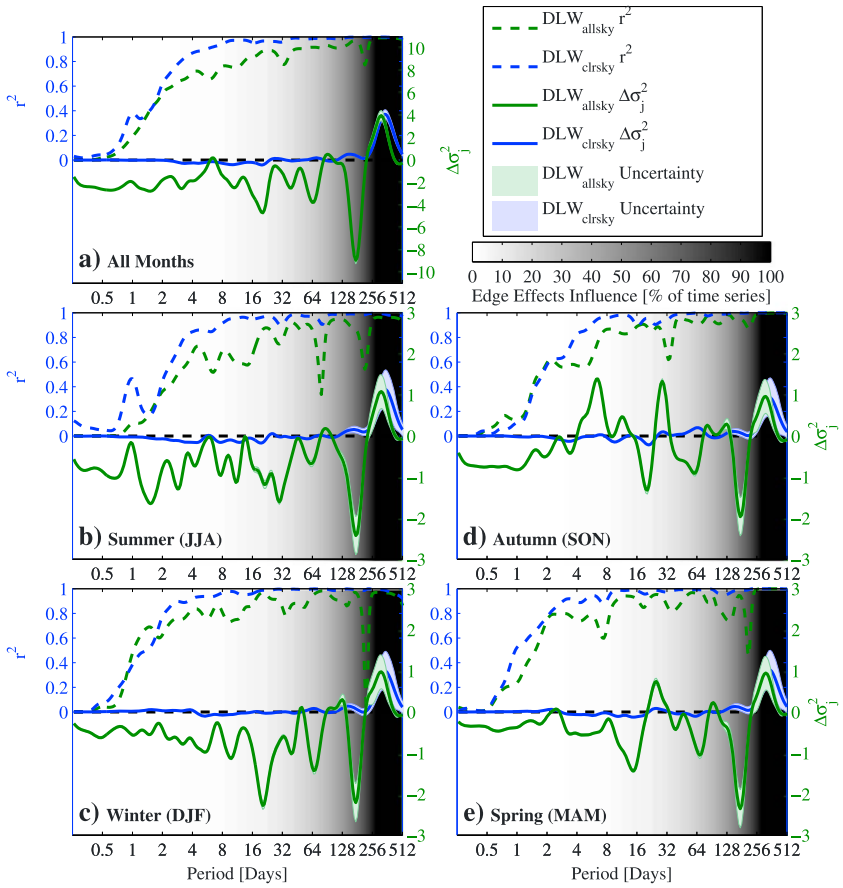

Figure 6. Squared correlation coefficient (r^2) as a function of period calculated between the time series of flux from surface-based observations and from ERA-Interim reanalysis data (dashed lines; *y* axes on the left column). Parameter r^2 is shown for the downwelling longwave all-sky flux (DLW_{allsky}, green) and the downwelling longwave clear-sky flux (DLW_{clrsky}, blue) for (a) all times, (b) summer, (c) winter, (d) autumn, and (e) spring. Also shown are the variance differences ($\Delta\sigma^2$; solid lines; *y* axis on the right column), as ERA-Interim minus surface-based observations, for both DLW_{allsky} and DLW_{clrsky}. The *x* axes are periods (on a $\log_2$ scale for readability). The gray scale shows the percentage of the time series at each scale influenced by edge effects (see text for a detailed description of the parameters and uncertainties).

At all times of the year, the correlation is near zero at periods from 0.25 to 0.5 days, then increases rapidly before stabilizing at high correlations (very close to 1) at periods near 2–6 days. This may represent the transition from local variability to time scales that represent spatial scales that can be resolved by ERA-Interim. These periods are consistent with the lags before the autocorrelation functions converge (Figure 5). The correlation stabilizes at smaller periods and to higher values in winter and spring compared to summer and autumn. DLW_{allsky} correlations are consistently lower than DLW_{clrsky} because of the additional uncertainty from clouds in ERA-Interim. In summer, there is an increase in correlation at a period of 1 day, corresponding to a good representation of the diurnal cycle.

Time scales varying over period <1 day are difficult to identify with the 3 h temporal resolution utilized in this study, and there is less signal to noise. For these periods, the correlation between ERA-Interim and surface-based observations approaches zero. However, this is not an artifact of the wavelet analysis or uncertainty in the observations as the correlation between the independent DLW_{allsky} surface-based observations (AERI and pyrgeometer) remains >0.85 (see Text S2 in the supporting information). From Figure 6a, the $\Delta\sigma_j^2$ for DLW_{allsky} (green line) reflects the finding that ERA-Interim typically underestimates the variance contributed by clouds. We conclude this because the $\Delta\sigma_j^2$ for DLW_{clrsky} (blue line) is near 0, consistent with the comparisons in section 4.1.1 and Figure 2. This is true even at short time scales, suggesting that the discrepancy arises from the forecast model. About 41% of the absolute value of $\Delta\sigma_j^2$ in DLW_{allsky} between ERA-Interim and the surface-based observations is confined to periods less than 6 days when the correlation

is also low. The remaining 59% of the absolute value of $\Delta\sigma_j^2$ is spread over longer time scales where the correlation is high, and we expect that most variability does not arise from local processes. Seventeen percent of the absolute value of DLW_{clrsky} $\Delta\sigma_j^2$ is also found between 6 days and 90 days (75% >90 days, 8% <6 days).

The two remaining features in $\Delta\sigma_j^2$ mark the semiannual and annual time scales at 16% and 8%, respectively, for the DLW_{allsky}. The width of the analyzing wavelet at these scales is large enough that edge effects are important, but note that edge effects are mostly subtractive. The errors are also observable in the raw data; smoothing the difference between the original time series (i.e., ERA-Interim minus surface-based observations) reveals periodicities at approximately 180 days in the DLW_{allsky} and 365 days in the DLW_{clrsky} with amplitudes of 5 to 10 W m^{-2}. Further examination of these features shows that the semiannual cycle in ERA-Interim is smaller than the surface-based observations, although the phasing is accurate (note that the correlation is high for these periods). The difference in the semiannual cycle is due to an underestimation of the cloud response to the semiannual cycle in ERA-Interim because this cycle is well represented by the ERA-Interim DLW_{clrsky}, but not DLW_{allsky}. The annual cycle in the DLW_{clrsky} is where most of the $\Delta\sigma_j^2$ in DLW_{clrsky} occurs; the DLW_{allsky} annual error is affected by this and shows a similar feature. The shift in the location of the DLW_{allsky} annual cycle $\Delta\sigma_j^2$ peak to a period smaller than 365 days may be an artifact of edge effects. However, differences in the seasonal representation of clouds in ERA-Interim could also produce this result by causing a phase shift in the seasonal cycle when compared to the surface-based observations. For both the DLW_{allsky} and DLW_{clrsky}, the differences in the annual cycle are positive (ERA-Interim has more variance), whereas most of the differences at other periods are negative.

We performed a sensitivity study to determine the influence that grid spatial resolution has on the results and found that the correlations are not sensitive to grid resolution, but the bias increases with coarser grid resolution. The sensitivity study is described in Text S1 in the supporting information.

In summary, the wavelet analysis shows that the $\Delta\sigma_j^2$ for periods smaller than the semiannual cycle, ERA-Interim generally underestimates the cloud radiative impact, most in summer and least in spring. The exception is autumn when ERA-Interim overestimates the cloud radiative impact at periods of approximately 6 days and 28 days.

4.3. Spatial Distribution of $DLW_{cldforce}$ Across the GrIS

In this section, the spatial distribution of $DLW_{cldforce}$ from ERA-Interim is analyzed in the context of the results from the previous sections. A sensitivity study was performed to determine how the results from the comparison at Summit may be extended for interpretation at other locations on the GrIS. The sensitivity study is described in Text S2 in the supporting information.

Figure 7 shows the average $DLW_{cldforce}$ across Greenland from ERA-Interim for all months and for each season. (Note that due to the characteristics of the $DLW_{cldforce}$ distributions, as shown in Figure 2, the average value does not necessarily coincide with the modal value). There are distinct patterns in the spatial distribution of $DLW_{cldforce}$ across the GrIS and noticeable differences in the patterns between seasons. In general, lower values shift from the northern GrIS in winter to the east in summer. In each season, the location of Summit (denoted with an "X") lies in a transition zone between relatively high $DLW_{cldforce}$ and relatively low $DLW_{cldforce}$. *Starkweather* [2004] also reported that Summit was positioned in a meridional transition zone for the net radiative effect of clouds, but Figure 7 indicates that this zone is spatially complex with respect to $DLW_{cldforce}$.

The spatial characteristics in all seasons appear closely tied to the topography of the ice sheet. Low values wrap around the edges of the north and east slopes. Higher values in the southeast appear in the relatively low elevation region (saddle) between the north and south domes in all seasons except summer. The annual average pattern (Figure 7a) corresponds closely to the pattern of annual average precipitation reported by *Ohmura and Reeh* [1991] if $DLW_{cldforce}$ is assumed to be positively correlated with precipitation. The fetch of air may be an important driver for the spatial pattern of $DLW_{cldforce}$, producing orographic effects that may explain the higher $DLW_{cldforce}$ on the windward (western) side and lower $DLW_{cldforce}$ on the leeward (eastern) side. Further investigations of winds at the cloud level are needed to confirm this, but it is consistent with the findings of *Ohmura and Reeh* [1991] who found a strong zonal gradient in summer with southwesterly 850 mb winds transecting the GrIS. *Ohmura and Reeh* [1991] also report a strong component of southeasterly winds traveling up the GrIS through the saddle in winter.

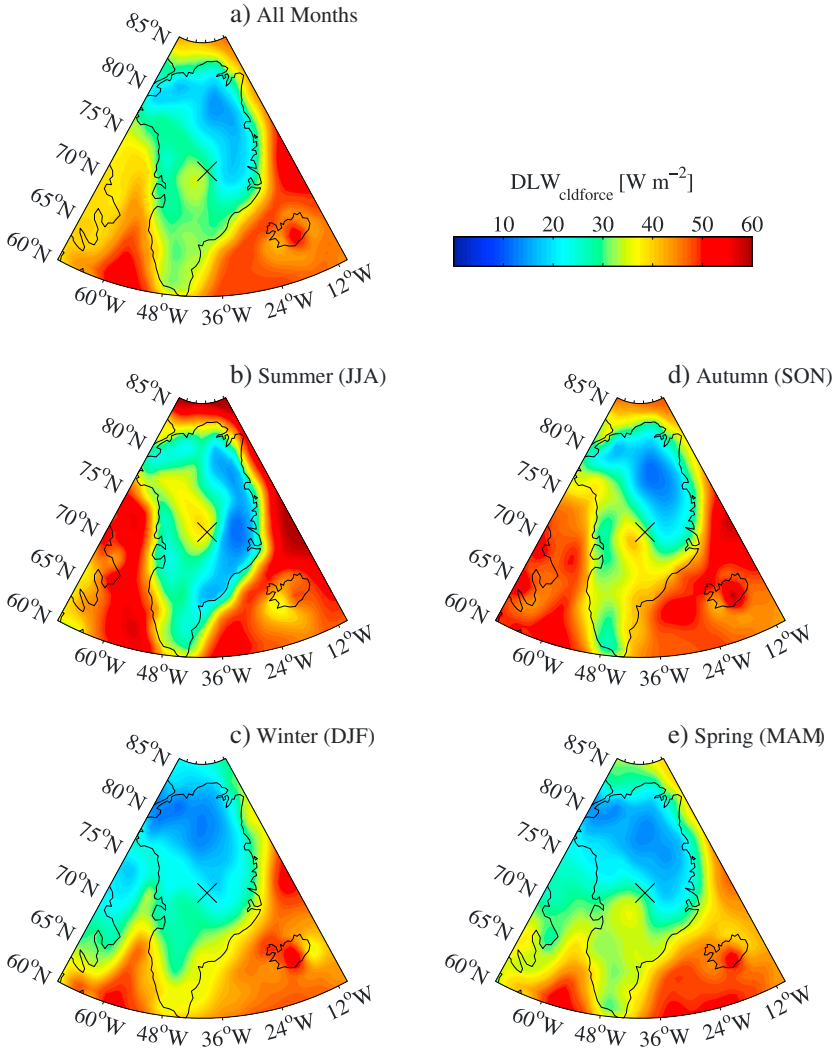

Figure 7. The average downwelling longwave cloud radiative forcing ($DLW_{cldforce}$) across Greenland for the July 2010 through August 2012 time period derived from ERA-Interim. Summit is marked with an X.

To better understand the representation of the thick clouds and thin clouds across the GrIS, fractional occurrence of $DLW_{cldforce}$ was calculated for two categories of $DLW_{cldforce}$ based qualitatively on Figure 2c, intermediate values ($20\,W\,m^{-2} < DLW_{cldforce} < 50\,W\,m^{-2}$) and high values ($DLW_{cldforce} > 50\,W\,m^{-2}$). Recall that intermediate and high values likely correspond to optically thin (or averages of clear and cloudy conditions over the 3 h period) and optically thick clouds, respectively. The results are shown in Figures 8 and 9. (Note that some of the smaller-scale variability in Figures 8 and 9 is nonphysical and appears to reflect the pattern of the grid. We believe that this nonphysical smaller-scale variability is associated with the net clear-sky longwave flux field, LW_{clrsky}, that was used to derive $DLW_{cldforce}$ from ERA-Interim, described in section 2.3 and that it is accentuated by category averaging in Figures 8 and 9). In general, ERA-Interim shows more intermediate $DLW_{cldforce}$ occurrences over the central ice sheet in the region near Summit (~30–35% of time) and fewer around the periphery (<25%), suggesting that orographic effects may influence the preference for thin clouds (Figure 8). In winter and spring when the higher frequencies of intermediate $DLW_{cldforce}$ are measured over Summit by both ERA-Interim and surface-observations, the higher frequencies are also found closer to the southwest coast as opposed to the north and northwest, as in summer and autumn.

The spatial patterns of thick clouds (Figure 9) more closely resemble the spatial patterns of the average $DLW_{cldforce}$ (Figure 7), in particular to the north and east where relatively few occurrences of high $DLW_{cldforce}$ (likely thick clouds) appear. In summer, there is a high frequency of high $DLW_{cldforce}$ values over the northwestern GrIS,

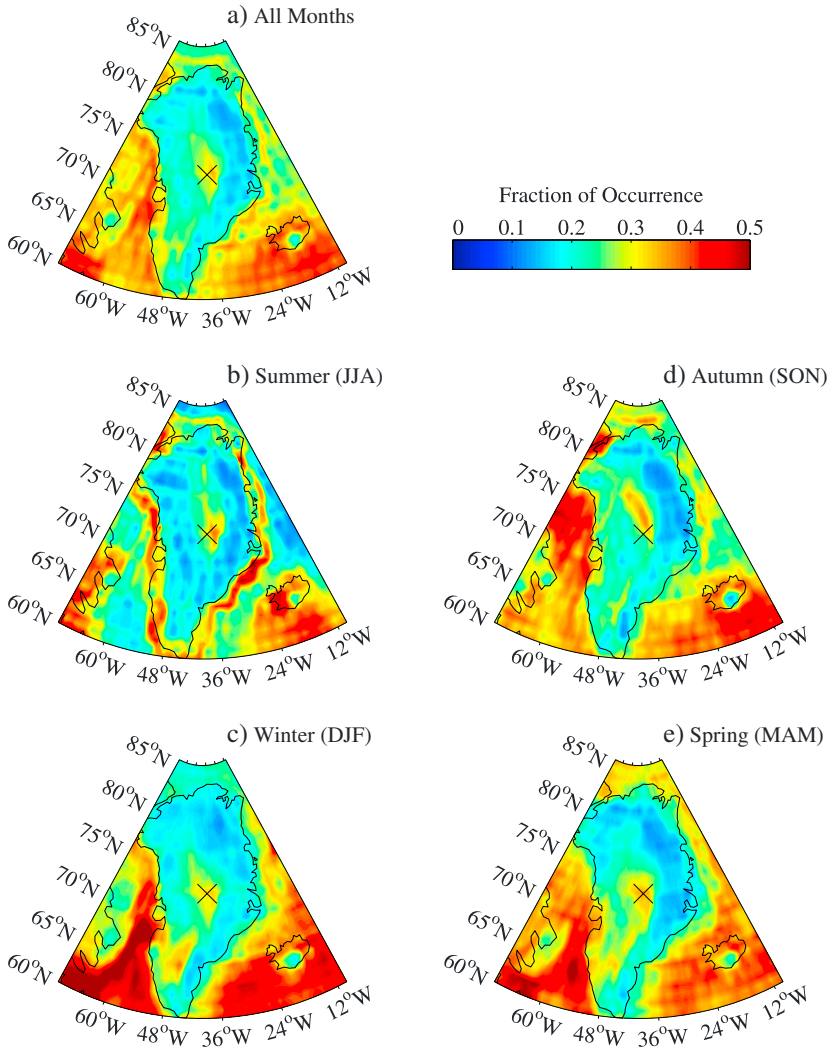

Figure 8. Fractional occurrence (in time) of intermediate downwelling longwave cloud radiative forcing ($DLW_{cldforce}$) ("intermediate" defined as $20\,m^{-2} < DLW_{cldforce} < 50\,W\,m^{-2}$) across Greenland for the July 2010 through August 2012 time period derived from ERA-Interim. Summit is marked with an X.

and Summit is situated at the edge of this feature. The transition between these locations corresponds to the dominant summer southwesterly wind patterns reported by *Ohmura and Reeh* [1991]. The actual frequency of large $DLW_{cldforce}$ at Summit is higher than is estimated by ERA-Interim, so it is likely that this feature spreads farther to the east than shown by ERA-Interim. In winter, and to some extent spring when ERA-Interim more accurately captures the frequency of high $DLW_{cldforce}$ at Summit, the transition zone has a weaker gradient across the central GrIS. Summit resides in the transition zone in autumn when the gradient is very strong.

5. Conclusions

In this study, we investigate the downwelling longwave flux (DLW) over Summit Station, Greenland, and across the Greenland Ice Sheet (GrIS). We utilize observations of all-sky DLW (DLW_{allsky}) and calculations of downwelling longwave clear-sky flux (DLW_{clrsky}) based on radiosonde observations and a radiative transfer model. Downwelling longwave cloud radiative forcing ($DLW_{cldforce}$), defined as $DLW_{allsky} - DLW_{clrsky}$, is also used. These are compared to the same fluxes from the ERA-Interim reanalysis for the study period of July 2010 through August 2012. An analysis of the DLW observations at Summit as well as an evaluation of the DLW in ERA-Interim are conducted using time-frequency decomposition (wavelet analysis), providing a more comprehensive approach that complements the basic statistical comparisons presented. By separating out

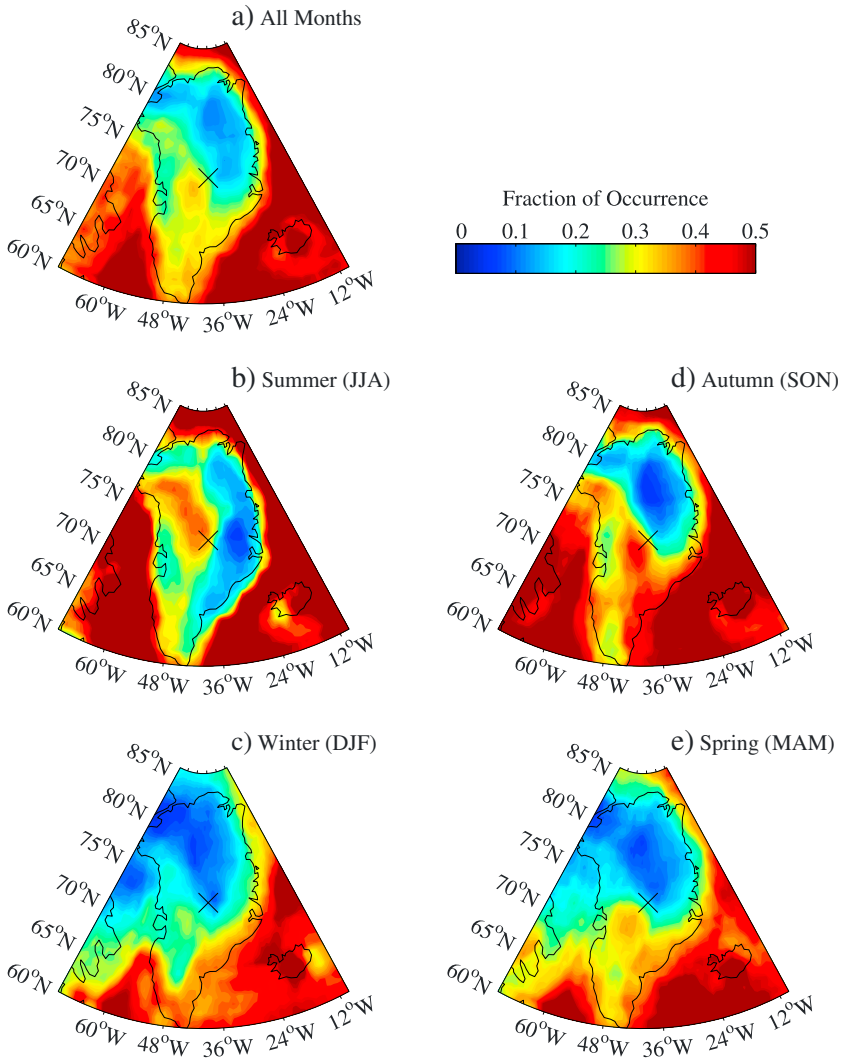

Figure 9. Fractional occurrence (in time) of the large downwelling longwave cloud radiative forcing ($DLW_{cldforce}$) ("large" defined as $DLW_{cldforce} > 50\ W\ m^{-2}$) across Greenland for the July 2010 through August 2012 time period derived from ERA-Interim. Summit is marked with an X. The dark red regions are fractional occurrences >0.5.

individual time scales of variability, this approach allows for these time scales to be examined separately. It therefore offers a way to examine some of the reasons for the differences between ERA-Interim and the surface-based observations. The evaluation and analysis are presented in parallel, providing mutually informative perspectives.

Using wavelet analysis, significant time scales of variability in DLW_{allsky} are identified at Summit. Synoptic-scale variability is generally not significant except in summer. Low-frequency variability (>2 weeks) is significant in all seasons. A shift in the low-frequency variability from 2 months to 2–4 weeks is seen as part of the seasonal shift from winter to summer. Power at periods between 6 and 12 days is lower than would be expected from the linearly damped, stochastically driven process of red noise calculated from the lag-1 autoregressive parameter. One mechanism for this is that 6 to 12 day variations of warm/moist/cloudy and cold/dry/clear conditions are relatively weak. Notably, there is a lack of significant high-frequency variability in the transition seasons, and variability may be acting over many time scales during these seasons. There is relatively little significant power beyond red noise at any of the time scales of variability between 8 and 64 days in autumn, suggesting that red noise is a good description of the variability for those time scales during that season. Spring is dominated by a strongly significant time scale of approximately 14 days, suggesting that episodes of clouds and episodes of clear sky persist for relatively long stretches of time in

spring. Many of these features are represented by ERA-Interim, and in fact, the wavelet power spectrum of DLW_{allsky} in ERA-Interim is qualitatively similar to the wavelet power spectrum from observations made at Summit. However, due to a larger lag-1 autocorrelation, statistical significance against a background of red noise is generally confined to periods between 0.5 and 4 days in ERA-Interim.

DLW_{clrsky} is reasonably well represented by ERA-Interim despite the fact that no surface-based observations over the GrIS were assimilated into the reanalysis during the study period. Overall, ERA-Interim underestimates the frequency of high $DLW_{cldforce}$ (likely optically thick clouds) and overestimates the frequency of clouds contributing to intermediate $DLW_{cldforce}$ (likely corresponding to optically thin clouds or variations of clear and cloudy conditions during the 3 h averaging period). The overestimation of intermediate values occurs mostly in summer, but the underestimation of large values occurs throughout the year. This results in an overall low bias in DLW_{allsky} and $DLW_{cldforce}$. The bias is mostly independent of time scale, so we propose that it is either due to cloud generation processes in ERA-Interim or persistent errors in the spatial positioning of air masses. As the DLW_{clrsky} is reasonably well represented by ERA-Interim, it is more likely the former.

The cloud response to the semiannual cycle is also underestimated by ERA-Interim, but the DLW_{clrsky} annual cycle (thus also the DLW_{allsky} annual cycle) is overestimated. Caution should be taken in interpreting the results of the semiannual and annual cycles in the study because of the influence of edge effects in the wavelet comparison. At shorter time scales, most periods show less variance in ERA-Interim. The lower variance corresponds to weaker amplitudes from transitions between warm/moist/cloudy and cold/dry/clear skies in ERA-Interim. Since the clear-sky component (DLW_{clrsky}) of the DLW_{allsky} is well represented by ERA-Interim, this result can be interpreted as corresponding to the low bias from clouds ($DLW_{cldforce}$) that was first identified through basic statistical comparisons in section 4.1.1. The main exception to the low bias occurs in autumn when variance at periods of ~1 week and 4 weeks is overestimated. This autumnal high bias may be associated with fluctuations in the stronger gradient in cloud properties across the transition zone near Summit during autumn compared to other seasons (Figure 8d), whereby ERA-Interim represents the location of Summit as being cloudier and more like the atmosphere to the south of Summit (Figure 8d) than is measured.

Time series reconstructions of the surface-based observations and ERA-Interim are highly correlated (>0.8) for longer time scales (>4 days), but correlations drop to near 0 at time scales less than ~4 days. The low correlations are likely associated with differences in the spatial resolutions of the data sets, which are more influential for short time scales. All of the time scales operate together in concert, so over the course of short time periods (e.g., 1 day), the time series of DLW in ERA-Interim generally follow the evolution of the signal measured at the surface. The wavelet comparisons show that this is driven mostly by time scales of variability operating on periods greater than 4 days. Thus, variations over shorter periods should not be expected to be accurately represented over the GrIS in ERA-Interim. This does not imply that the reanalysis cannot determine the surface energy budget correctly. Unbiased yet uncorrelated high-frequency variability could still yield an unbiased estimate of the surface energy budget in much the same way that this is possible with measurements averaged over time.

Recent research has confirmed that a major contributor to $DLW_{cldforce}$ in the Arctic, liquid water in mixed-phase and liquid-only clouds, is being underestimated by ERA-Interim at Summit [*Bennartz et al*., 2013]. Therefore, it is likely that the biases in cloud liquid water content are closely tied to the biases in DLW shown in this paper. However, biases in clouds from models have also been tied to errors in the surface-based temperature inversion [*Pithan et al*., 2013]. Further investigations are needed to see if the DLW biases in ERA-Interim highlighted in this work could be tied to other biases, such as low-level stability. If the source of the ERA-Interim error is related to larger spatial scale dynamics or low-level stability, the assimilation of radiosondes launched from Summit may be sufficient to correct the problem, and future comparisons using reanalysis data that include assimilations from Summit can assess this.

An analysis of the spatial distribution of $DLW_{cldforce}$ over the GrIS from ERA-Interim revealed that Summit is located in a narrow transition zone of cloud radiative effects. Typically, lower $DLW_{cldforce}$ occurs to the north and east, while higher $DLW_{cldforce}$ occurs to the southeast over the saddle between the north and south domes. The orientation of the transition zone is seasonally dependent and most complex in autumn when ERA-Interim exhibits competing biases in the cloud variability at different time scales. If clouds are indeed thinner (or clear sky dominates) over the north and eastern regions of the GrIS, ERA-Interim may be expected

to perform better in those locations. The spatial patterning is also more closely controlled by the occurrence of high $DLW_{cldforce}$ than intermediate $DLW_{cldforce}$. Orographic influences may be associated with the high frequency of thin clouds in ERA-Interim over the high elevations of the ice sheet. The pattern in high $DLW_{cldforce}$ corresponds to previous research of the 850 mb wind direction and precipitation by *Ohmura and Reeh* [1991]. Future research should identify connections between these processes and the transition zone if they exist.

Acknowledgments

This research was supported by National Science Foundation grants ARC-0856773, 0904152 and 0856559 as part of the Arctic Observing Network. ICECAPS data sets are available from the U.S. Department of Energy Atmospheric Radiation Measurement program data archive (http://www.arm.gov). Pyrgeometer measurements were provided by the University of Colorado/CIRES (Steffen Research Group). We thank the team of scientists, engineers, field technicians, and students that are part of the ICECAPS team and Polar Field Services for their logistical support at Summit Station. Additional observational data used in this study were provided by NOAA ESRL Global Monitoring Division (P.P. Tans, J. Elkins, J. Butler, S. Montzka, and T. Thompson). Computational support for wavelet analysis was provided by C. Torrence (http://paos.colorado.edu/research/wavelets/). Meteorological data used in flux calculations were provided by NOAA-ESRL. We are thankful for the contributions from the anonymous reviewers, which helped to improve the manuscript. G. Compo received support from the U.S. Department of Energy Office of Science Biological and Environmental Research program and from the NOAA Climate Program Office. C. Cox received support through the CIRES Visiting Fellowship Program and the University of Idaho and logistical support from NOAA-ESRL. P. Rowe received support from NSF award ARC-1108451 and from Proyecto Basal (Preis USA-1298), USACH-DICYT ASOCIATIVO (Preis 041331CC_DAS), and USACH-DICYT Postdoc. Intellectual contributions were made by G. de Boer (CIRES, University of Colorado, NOAA-ESRL), J. Abatzoglou (University of Idaho), and J. Hicke (University of Idaho). Data support was provided by D.D. Turner (University of Oklahoma, NOAA-NSSL). Walden would like to acknowledge conversations with M. Town and I. Gorodetskaya (KU Leuven) that inspired this work.

References

Alley, R. B., P. U. Clark, P. Huybrechts, and I. Joughin (2005), Ice-sheet and sea-level changes, *Science*, *310*, 456–460, doi:10.1126/science.1114613.

Bennartz, R., M. D. Shupe, D. D. Turner, V. P. Walden, K. Steffen, C. J. Cox, M. S. Kulie, N. B. Miller, and C. Pettersen (2013), July 2012 Greenland melt extent enhanced by low-level liquid clouds, *Nature*, *496*, 83–86, doi:10.1038/nature11997.

Box, J. E. (2013), Greenland ice sheet mass balance reconstruction. Part II: Surface mass balance (1840–2010), *J. Clim.*, *26*, 6974–6989, doi:10.1175/JCLI-D-00518.1.

Bromwich, D. H., R. L. Fogt, K. I. Hodges, and J. E. Walsh (2007), A tropospheric assessment of the ERA-40, NCEP, and JRA-25 global reanalyses in the polar regions, *J. Geophys. Res.*, *112*, D10111, doi:10.1029/2006JD007859.

Clough, S. A., and M. J. Iacono (1995), Line-by-line calculation of atmospheric fluxes and cooling rates 2. Application to carbon dioxide, ozone, methane, nitrous oxide, and the halocarbons, *J. Geophys. Res.*, *100*, 16,519–16,535, doi:10.1029/95JD01386.

Clough, S. A., M. J. Iacono, and J.-L. Moncet (1992), Line-by-line calculations of atmospheric fluxes and cooling rates: Application to water vapor, *J. Geophys. Res.*, *97*, 15,761–15,785, doi:10.1029/92JD01419.

Conway, T. J., P. M. Lang, and K. A. Masarie (2011), Atmospheric carbon dioxide dry air mole fractions from the NOAA ESRL Carbon Cycle Cooperative Global Air Sampling Network, 1968–2010, Version: 2011–0621. [Available at ftp://ftp.cmdl.noaa.gov/ccg/co2/flask/month.]

Cox, C. J. (2013), Clouds across the Arctic: A spatial perspective uniting surface observations of downwelling infrared radiation, reanalyses and education, PhD dissertation, Evironmental Sci. Prog., Univ. of Idaho, Moscow, Idaho.

Cox, C. J., V. P. Walden, and P. M. Rowe (2012), A comparison of atmospheric conditions at Eureka, Canada and Barrow, Alaska (2006–2008), *J. Geophys. Res.*, *117*, D12204, doi:10.1029/2011JD017164.

Cox, C. J., D. D. Turner, P. M. Rowe, M. D. Shupe, and V. P. Walden (2014), Cloud microphysical properties retrieved from downwelling infrared radiance measurements made at Eureka, Nunavut, Canada (2006–09), *J. Appl. Meteorol. Climatol.*, *53*, 772–791, doi:10.1175/JAMC-D-13-0113.1.

Curry, J. A., W. B. Rossow, R. Randall, and J. L. Schramm (1996), Overview of Arctic cloud radiation characteristics, *J. Clim.*, *9*, 1731–1764, doi:10.1175/1520-8560442(1996)009<1731:OOACAR>2.0.CO;2.

de Boer, G., E. W. Eloranta, and M. D. Shupe (2009), Arctic mixed-phase stratiform cloud properties from multiple years of surface-based measurements at two high-latitude locations, *J. Atmos. Sci.*, *66*, 2874–2887, doi:10.1175/2009JAS3029.1.

de Boer, G., M. D. Shupe, P. M. Caldwell, S. E. Bauer, O. Persson, J. S. Boyle, M. Kelley, S. A. Klein, and M. Tjernström (2014), Near-surface meteorology during the Arctic Summer Cloud Ocean Study (ASCOS): Evaluation of reanalyses and global climate models, *Atmos. Chem. Phys.*, *14*, 427–445, doi:10.5194/acp-14-427-2014.

Dee, D. P., et al. (2011), The ERA-Interim reanalysis: Configuration and performance of the data analysis system, *Q. J. R. Meteorol. Soc.*, *137*, 553–597, doi:10.1002/qj.828.

Dlugokencky, E. J., P. M. Lang, and K. A. Masarie (2010), Atmospheric methane dry air mole fractions from the NOAA ESRL Carbon Cycle Cooperative Global Air Sampling Network, 1983–2009, Version: 2010-08-12. [Available at ftp://ftp.cmdl.noaa.gov/ccg/ch4/flask/event.]

Dong, X., and G. G. Mace (2003), Arctic stratus cloud properties and radiative forcing derived from ground-based data collected at Barrow, Alaska, *J. Clim.*, *16*, 445–461, doi:10.1175/1520-0442(2003)016<0445:ASCPAR>2.0.CO;2.

Dong, X., B. Xi, K. Crosby, C. N. Long, R. S. Stone, and M. D. Shupe (2010), A 10 year climatology of Arctic cloud fraction and radiative forcing at Barrow, Alaska, *J. Geophys. Res.*, *115*, D17212, doi:10.1029/2009JD013489.

Doran, J. C., J. C. Barnard, and W. J. Shaw (2006), Modification of summertime Arctic cloud characteristics between a coastal and inland site, *J. Clim.*, *19*, 3207–3219.

Farge, M. (1992), Wavelet transforms and their applications to turbulence, *Annu. Rev. Fluid Mech.*, *24*, 395–457, doi:10.1146/annurev.fluid.24.1.395.

Fichefet, T., C. Poncin, H. Goosse, P. Huybrechts, I. Janssens, and H. Le Treut (2003), Implications of changes in freshwater flux from the Greenland ice sheet for the climate of the 21st century, *J. Geophys. Res. Lett.*, *30*(17), 1911, doi:10.1029/2003GL017826.

Francis, J. A., and E. Hunter (2006), New insight into the disappearing Arctic sea ice, *Eos Trans. AGU*, *87*, 509–511, doi:10.1029/2006EO460001.

Francis, J. A., and E. Hunter (2007), Changes in the fabric of the Arctic's greenhouse blanket, *Environ. Res. Lett.*, *2*, 04511, doi:10.1088/1748-9326/2/4/045011.

Hanna, E., P. Huybrechts, K. Steffen, J. Cappelen, R. Huff, C. Shuman, T. Irvine-Fynn, S. Wise, and M. Griffiths (2008), Increased runoff from melt from the Greenland Ice Sheet: A response to global warming, *J. Clim.*, *21*, 331–341, doi:10.1175/2007JCLI1964.1.

Intrieri, J. M., C. W. Fairall, M. D. Shupe, P. O. G. Persson, E. L. Andreas, P. S. Guest, and R. E. Moritz (2002), An annual cycle of Arctic surface cloud forcing at SHEBA, *J. Geophys. Res.*, *107*(C10), 8039, doi:10.1029/2000JC000439.

Knuteson, R. O., et al. (2004a), Atmospheric Emitted Radiance Interferometer. Part I: Instrument design, *J. Atmos. Oceanic Technol.*, *21*, 1763–1776, doi:10.1175/JTECH-1662.1.

Knuteson, R. O., et al. (2004b), Atmospheric Emitted Radiance Interferometer. Part II: Instrument performance, *J. Atmos. Oceanic Technol.*, *21*, 1777–1789, doi:10.1175/JTECH-1663.1.

Lesins, G., L. Bourdages, T. J. Duck, J. R. Drummond, E. W. Eloranta, and V. P. Walden (2009), Large surface radiative forcing from topographic blowing snow residuals measured in the High Arctic at Eureka, *Atmos. Chem. Phys.*, *9*, 1847–1862, doi:10.5194/acp-9-1847-2009.

Liu, Y., J. R. Key, and X. Wang (2008), The influence of changes in cloud cover on recent surface temperature trends in the Arctic, *J. Clim.*, *21*, 705–715, doi:10.1175/2007JCLI1681.1.

Liu, Y., J. R. Key, S. A. Ackerman, G. G. Mace, and Q. Zhang (2012), Arctic cloud macrophysical characteristics from CloudSat and CALIPSO, *Remote Sens. Environ.*, *124*, 159–173, doi:10.1016/j.rse.2012.05.006.

Long, C. N., and Y. Shi (2008), An automated quality assessment and control algorithm for surface radiation measurements, *Open Atmos. Sci. J.*, *2*, 23–37, doi:10.2174/1874282300802010023.

Mariani, Z., et al. (2012), Infrared measurements in the Arctic using two Atmospheric Emitted Radiance Interfermometers, *Atmos. Meas. Technol.*, *5*, 328–344, doi:10.5194/amt-5-329-2012.

McClatchey, R. A., R. W. Fenn, J. E. A. Selby, F. E. Holtz, and J. S. Garing (1972), Optical properties of the atmosphere, Tech. Rep. *AFCRL-72-0497*, 3rd ed., 108 pp., Air Force Geophys. Lab., Hanscom AFB, Mass.

Meyers, S. D., B. G. Kelly, and J. J. O'Brien (1993), An introduction to wavelet analysis in oceanography and meteorology: With applications to the dispersion of Yanai waves, *Mon. Weather Rev.*, *121*, 2858–2866.
Miller, N. B., D. D. Turner, R. Bennartz, M. D. Shupe, M. S. Kulie, M. P. Caddedu, and V. P. Walden (2013a), Surface-based inversions above central Greenland, *J. Geophys. Res. Atmos.*, *118*, 495–506, doi:10.1029/2012JD018867.
Miller, N., V. P. Walden, D. D. Turner, M. D. Shupe, R. Bennartz, C. Pettersen, M. Kulie, C. J. Cox, and B. Castellani (2013b), Extreme events at Summit, Greenland: 3 days, 3 years and 33 summers, paper presented at 12th Conference on Polar Meteorology and Oceanography Am. Meteorol. Soc., Seattle, Wash.
Morrison, H., G. de Boer, G. Feingold, J. Harrington, M. D. Shupe, and K. Sulia (2012), Resilience of persistent Arctic mixed-phase clouds, *Nat. Geosci.*, *5*, 11–17, doi:10.1038/NGEO1332.
Neff, W., G. P. Compo, R. M. Ralph, and M. D. Shupe (2014), Continental heat anomalies and the extreme melting of the Greenland ice surface in 2012 and 1889, *J. Geophys. Res. Atmos.*, *119*, 6520–6536, doi:10.1002/2014JD021470.
Ohmura, A., and N. Reeh (1991), New precipitation and accumulation maps for Greenland, *J. Glaciol.*, *37*, 140–148.
Ohmura, A., et al. (1998), Baseline Surface Radiation Network (BSRN/WCRP): New precision radiometry for climate research, *Bull. Am. Meteorol. Soc.*, *79*, 2115–2136, doi:10.1175/1520-0477(1998)079<2115:BSRNBW>2.0.CO;2.
Osterkamp, T. E. (2007), Characteristics of the recent warming of permafrost in Alaska, *J. Geophys. Res.*, *112*, F02S02, doi:10.1029/2006JF000578.
Overland, J. E., M. Wang, and S. Salo (2008), The recent Arctic warm period, *Tellus A*, *60*, 589–597, doi:10.1111/j.1600-0870.2008.00327.x.
Parkinson, C. L., and J. C. Comiso (2013), On the 2012 record low Arctic sea ice cover: Combined impact of preconditioning and an August storm, *Geophys. Res. Lett.*, *40*, 1–6, doi:10.1002/grl.50349.
Pithan, F., B. Medeiros, and T. Mauritsen (2013), Mixed-phase clouds cause climate model biases in Arctic wintertime temperature inversions, *Clim. Dyn.*, *43*(1–2), 289–303, doi:10.1007/s00382-013-1964-9.
Rignot, E., and P. Kanagaratnam (2006), Changes in the velocity structure of the Greenland Ice Sheet, *Science*, *311*, 986–990, doi:10.1126/science.1121381.
Rignot, E., J. E. Box, E. Burgess, and E. Hanna (2008), Mass balance of the Greenland ice sheet from 1958–2007, *Geophys. Res. Lett.*, *35*, L20502, doi:10.1029/2008GRL035417.
Rowe, P. M., S. P. Neshyba, and V. P. Walden (2011a), Responsivity-based criterion for accurate calibration of FTIR emission spectra: Theoretical development and bandwidth estimation, *Opt. Express*, *19*, 5451–5463, doi:10.1364/OE.19.005451.
Rowe, P. M., S. P. Neshyba, C. J. Cox, and V. P. Walden (2011b), A responsivity-based criterion for accurate calibration of FTIR emission spectra: Identification of in-band low-responsivity wavenumbers, *Opt. Express*, *19*, 5930–5941, doi:10.1364/OE.19.005930.
Schuur, E. A. G., et al. (2008), Vulnerability of permafrost carbon to climate change: Implications for the global carbon cycle, *BioScience*, *8*, 701–714, doi:10.1641/B580807.
Shupe, M. D. (2011), Clouds at Arctic atmospheric observatories. Part II: Phase characteristics, *J. Appl. Meteorol. Climatol.*, *50*, 645–661, doi:10.1175/2010JAMC2468.1.
Shupe, M. D., and J. M. Intrieri (2004), Cloud radiative forcing of the Arctic surface: The influence of cloud properties, surface albedo, and solar zenith angle, *J. Clim.*, *17*, 616–628, doi:10.1175/1520-0442(2004)017<0616:CRFOTA>2.0.CO;2.
Shupe, M. D., V. P. Walden, E. Eloranta, T. Uttal, J. R. Campbell, S. M. Startweather, and M. Shiobara (2011), Clouds at Arctic atmospheric observatories. Part I: Occurrence and macrophysical properties, *J. Appl. Meteorol. Climatol.*, *50*, 626–644, doi:10.1175/2010JAMC2467.1.
Shupe, M. D., et al. (2013), High and dry: New observations of tropospheric and cloud properties above the Greenland Ice Sheet, *Bull. Am. Meteorol. Soc.*, *94*, 169–186, doi:10.1175/BAMS-D-11-00249.1.
Stamnes, K., S.-C. Tsay, W. Wiscombe, and K. Jayaweera (1988), Numerically stable algorithm for discrete-ordinate-method radiative transfer in multiple scattering and emitting layered media, *Appl. Opt.*, *27*, 2502–2509, doi:10.1364/AO27.002502.
Starkweather, S. M. (2004), Characteristics of cloud cover and its radiative impacts over high elevations of the Greenland ice sheet, PhD dissertation, Dep. Atmos. and Oceanic Sci., Univ. of Colo., Boulder.
Stramler, K., A. Del Genio, and W. Rossow (2011), Synoptically driven Arctic winter States, *J. Clim.*, *47*, 1747–1762, doi:10.1175/2010JCLI3817.1.
Torrence, C., and G. P. Compo (1998), A practical guide for wavelet analysis, *Bull. Am. Meteorol. Soc.*, *79*, 61–78, doi:10.1175/1520-0477(1998)079<0061:APGTWA>2.0.CO;2.
Town, M. S., V. P. Walden, and S. G. Warren (2005), Spectral and broadband longwave downwelling radiative fluxes, cloud radiative forcing, and fractional cloud cover over the South Pole, *J. Clim.*, *18*, 4235–4252, doi:10.1175/JCLI3525.1.
Turner, D. (2005), Arctic mixed-phase cloud properties from AERI lidar observations: Algorithm and results from SHEBA, *J. Appl. Meteorol.*, *44*, 427–444, doi:10.1175/JAM2208.1.
Walsh, J. E., and W. L. Chapman (1998), Arctic cloud-radiation-temperature associations in observational data and atmospheric reanalyses, *J. Clim.*, *11*, 3030–3045, doi:10.1175/1520-00442(1998)011<3030:ACRTAI>2.0.CO;2.
Walsh, J. E., W. L. Chapman, and D. H. Portis (2009), Arctic cloud fraction and radiative fluxes in atmospheric reanalyses, *J. Clim.*, *22*, 2316–2334, doi:10.1175/2008JCLI2213.1.
Wang, J., J. Zhang, E. Watanabe, M. Ikeda, K. Mizobata, J. E. Walsh, X. Bai, and B. Wu (2009), Is the Dipole Anomaly a major driver to record lows in Arctic summer sea ice extent, *Geophys. Res. Lett.*, *36*, L05706, doi:10.1029/2008GL036706.
Wang, M., and J. E. Overland (2009), A sea ice free summer Arctic within 30 years?, *Geophys. Res. Lett.*, *36*, L0752, doi:10.1029/2009GL037820.
Wang, X., and J. R. Key (2005a), Arctic surface, cloud, and radiation properties based on the AVHRR Polar Pathfinder dataset. Part I: Spatial and temporal characteristics, *J. Clim.*, *18*, 2558–2574, doi:10.1175/JCLI3438.1.
Wang, X., and J. R. Key (2005b), Arctic surface, cloud, and radiation properties based on the AVHRR Polar Pathfinder dataset. Part II: Recent trends, *J. Clim.*, *18*, 2575–2593, doi:10.1175/JCLI3439.1.
Zhang, J., R. Lindsay, A. Schweiger, and M. Steele (2013), The impact of an intense summer cyclone on 2012 Arctic sea ice retreat, *Geophys. Res. Lett.*, *40*, 720–726, doi:10.1002/grl.50190.
Zhang, X., A. Sorteberg, J. Zhang, R. Gerdes, and J. C. Comiso (2008), Recent radical shifts of atmospheric circulations and rapid changes in Arctic climate system, *Geophys. Res. Lett.*, *35*, L22701, doi:10.1029/2008GL035607.